RSC Advances

PAPER

View Article Online
View Journal | View Issue

Cite this: *RSC Adv.*, 2026, **16**, 11918

Photoluminescence and thermoluminescence properties of Er^{3+} doped $MgGa_2O_4$ nanoparticles: a dual-mode visible-NIR phosphor for optoelectronic and dosimetric applications

Jyothi T. P,[abc] Kartik Gopal,[ab] Lavanya D. R,[ab] A. P. Gnana Prakash[d] and Sunitha D. V *[ab]

Er^{3+}-doped $MgGa_2O_4$ nanoparticles with varying concentrations (0–9 mol%) were synthesized using the self-combustion method and systematically analyzed for structural, optical, and dosimetry performance. XRD confirmed a single-phase cubic spinel structure (JCPDS 10-0113), while SEM, EDX, and HRTEM revealed uniformly distributed nanocrystals (~51 nm) with homogeneous composition. UV-vis diffuse reflectance spectra showed a band gap decrease from 5.17 to 4.86 eV with increasing Er^{3+}, attributed to defect-induced band tailing. FTIR confirmed characteristic Mg–O and Ga–O vibrations, validating structural integrity. Photoluminescence studies exhibited intense green ($^4S_{3/2} \rightarrow {}^4I_{15/2}$) and NIR ($^4I_{13/2} \rightarrow {}^4I_{15/2}$) emissions, with maximum intensity, extended lifetime (3.2 ns), and high quantum yield (58.29%) at 3 mol% Er^{3+}. CIE and CCT analyses placed the emission in the green-yellow region having CCT ~5291 K, suitable for WLEDs. Thermoluminescence (TL) glow curves displayed a single prominent peak at ~200 °C, with highest intensity for 5 mol% Er^{3+} at 5 kGy dose, corresponding to medium-depth traps (E = 0.9–1.0 eV). Deconvolution revealed two trap types: shallow (oxygen vacancies) and deep (Er^{3+}–V_O/Er^{3+}–Ga^+ complexes). The synergistic optical and TL performance confirms $MgGa_2O_4$:Er^{3+} as a promising multifunctional phosphor for WLED and γ-ray dosimetry applications.

Received 16th November 2025
Accepted 19th December 2025

DOI: 10.1039/d5ra08839a

rsc.li/rsc-advances

1 Introduction

Inorganic oxide-based phosphor materials have become central to recent advancements in photonics, optoelectronics, and radiation sensing applications,[1–5] owing to their excellent chemical durability, thermal stability, and capacity to host rare-earth ions within robust crystalline frameworks.[6–8] Among these, magnesium gallate ($MgGa_2O_4$), a normal spinel oxide, has emerged as a particularly attractive host matrix due to its wide bandgap (~4.5–5.0 eV), low phonon energy, and high resistance to moisture and radiation-induced damage.[9–11] These features render $MgGa_2O_4$ a compelling platform for the incorporation of optically active dopants, particularly lanthanide ions, to tailor emission properties for specific device-level applications such as persistent luminescence, thermoluminescence dosimetry, and solid-state lighting.[12–15]

Rare-earth (RE^{3+}) ions, owing to their 4f electronic configuration, exhibit sharp intra-4f transitions, high color purity, and long-lived excited states, making them indispensable in the design of next-generation phosphors.[16–18] Erbium (Er^{3+}) is of particular interest due to its emission bands spanning visible (green: ~550 nm) and near-infrared (~1.54 μm) regions, which are vital for applications in optical amplifiers, upconversion devices, and bio-imaging.[19–21] However, the efficiency of Er^{3+}-activated emission is critically influenced by the host lattice, dopant distribution, local symmetry, and phonon interactions. Although Er^{3+} has been widely studied in silicate, fluoride,[22,23] and garnet systems,[24] its incorporation into gallate-based spinels remains relatively underexplored,[25] especially in the context of phase-pure, nanocrystalline hosts synthesized *via* combustion methods.

Furthermore, an essential challenge in designing high-performance RE^{3+}-doped phosphors lies in achieving homogenous dopant dispersion at the nanoscale while avoiding concentration quenching, a phenomenon arising from energy transfer between closely spaced dopant ions, leading to non-radiative decay.[26–30] Optimal dopant concentration must be carefully tuned to balance luminescent efficiency and structural integrity. Yet, there exists a lack of systematic studies evaluating the effect of progressive Er^{3+} doping on the structural,

[a]*Department of Physics, School of Applied Sciences, REVA University, Bengaluru-560064, Karnataka, India. E-mail: sunitha.dv@reva.edu.in; Tel: +91-7760884884*

[b]*Center for Advance Materials and Research in Physics, REVA Research Center, REVA University, Bengaluru-560064, Karnataka, India*

[c]*Government First Grade College, KR Puram, Bengaluru, 560036, Karnataka, India*

[d]*Department of Studies in Physics, University of Mysore, Manasagangotri, Mysore-06, Karnataka, India*

morphological, and optical characteristics of $MgGa_2O_4$, particularly in the nanoscale regime.

Conventional ceramic routes for phosphor synthesis often necessitate prolonged calcination at elevated temperatures (>1200 °C), which can result in coarse grain formation, phase impurities, and dopant clustering.[31,32] To circumvent these limitations, solution combustion synthesis (SCS),[33] has gained attention as a rapid, energy-efficient method capable of producing highly dispersed, nanocrystalline oxides with controlled stoichiometry. SCS utilizes a self-sustaining exothermic redox reaction between metal nitrates (oxidizers) and organic fuels, such as urea, to yield voluminous, foamy powders within minutes. The inherent rapidity and localized heating in SCS foster phase-pure formation and homogeneous doping, making it well-suited for synthesizing luminescent nanophosphors with tailored functionalities.[34,35]

While previous studies have reported Dy^{3+}, Eu^{3+}, and Mn^{2+}-doped $MgGa_2O_4$ phosphors with promising emission properties,[36] detailed insight into Er^{3+} doping remains limited, especially with respect to synthesis *via* combustion methods and subsequent evaluation of emission behavior across different dopant concentrations. Understanding how Er^{3+} ions integrate into the spinel lattice, modify crystallographic parameters, and influence photoluminescence is crucial for developing phosphors tailored for specific spectral outputs and application domains such as white light-emitting diodes (WLEDs) and radiation dosimeters.[37,38]

In this context, the present study focuses on the systematic synthesis and characterization of $MgGa_2O_4$ nanoparticles doped with varying concentrations of Er^{3+} ions (1–9 mol%) *via* solution combustion synthesis. The structural phase purity, lattice distortion effects, particle morphology, and luminescent behavior were thoroughly investigated as a function of Er^{3+} content. The influence of dopant-induced crystallographic disorder and local field effects on the green emission intensity and spectral features was explored to establish optimal doping regimes for efficient optical output. These findings contribute to a deeper understanding of the host–dopant interactions in spinel gallates and expand the applicability of $MgGa_2O_4$:Er^{3+} systems in emerging optoelectronic and dosimetry applications.

2 Experimental methods

2.1 Materials

99.99% pure magnesium nitrate hexahydrate ($Mg(NO_3)_2 \cdot 6H_2O$), gallium nitrate hexahydrate ($Ga(NO_3)_3 \cdot 6H_2O$), erbium nitrate hexahydrate ($Er(NO_3)_3 \cdot 6H_2O$) and urea (NH_2CO_2NH) were procured from Sigma-Aldrich. The raw materials procured are of analytical grade and were used directly for material preparation without further purification.

2.2 Procedure for the experimentation

$MgGa_2O_4$ nanoparticles with different Er^{3+} concentrations (1, 3, 5, 7, and 9 mol%) were prepared using the SCS method. During the synthesis, a stoichiometric oxidizer-to-fuel ratio of 1 : 1 was maintained using $Mg(NO_3)_2 \cdot 6H_2O$, $Ga(NO_3)_3 \cdot 6H_2O$, $Er(NO_3)_3 \cdot 6H_2O$, and NH_2CONH_2 as precursors. These materials were completely dissolved in 20 mL of double-distilled water under continuous stirring for 20 min to obtain a homogeneous solution. The resulting solution was transferred to a silica crucible and placed in a preheated muffle furnace at 500 °C, where a rapid exothermic combustion reaction occurred within 5 min, producing a voluminous, foamy white powder. The obtained product was finely ground using an agate mortar and pestle to ensure uniform particle size. Subsequently, the powder was calcined at 1000 °C for 4 hours to achieve highly crystalline and phase-pure $MgGa_2O_4$:Er^{3+} nanoparticles. This synthesis process was repeated for each Er^{3+} doping concentration. The resulting nanoparticles were then analyzed for their structural, morphological, and luminescent characteristics to evaluate their potential applications in white light-emitting diodes (WLEDs) and radiation dosimetry.

2.3 Characterization methods

The structural and phase composition of $MgGa_2O_4$:Er^{3+} (0–9 mol%) nanoparticles were characterized using a Rigaku Smart Lab Powder X-ray diffractometer (PXRD) with Cu-Kα radiation (λ = 1.541 Å). XRD data were collected over a 2θ range of 20–80° at a scanning rate of 2° min^{-1} to verify phase purity and crystallinity. Fourier-transform infrared (FTIR) spectra were obtained using a Bruker Alpha-II spectrophotometer operating in the 4000–400 cm^{-1} range with a resolution of 0.9 cm^{-1}. Measurements were performed in both transmission and attenuated total reflectance (ATR) modes with a KBr beam splitter to identify vibrational modes and bonding features. Surface morphology and elemental composition were analyzed using a VEGA3 TESCAN scanning electron microscope (SEM) operating at 0.2–30 kV, coupled with an energy-dispersive X-ray (EDX) system to determine particle size, shape, and elemental distribution. Optical absorption spectra were recorded using a Thermo Scientific UV-visible spectrophotometer in the 200–800 nm wavelength range to study bandgap energy and optical transitions. Photoluminescence (PL) analyses, including lifetime decay, quantum yield, and thermal stability, were carried out using an FLS1000 Edinburgh Instrument. Excitation sources included a 450 W Xenon arc lamp (250–900 nm) and a 200 mW He–Cd LASER (325 nm). Time-resolved PL measurements employed microsecond flash lamps and pulsed lasers/LEDs at various wavelengths to investigate decay kinetics. Emission spectra were detected using visible PMT 900 and NIR PMT 1700 detectors to comprehensively evaluate the luminescent performance for WLED applications. Thermoluminescence (TL) studies were performed at room temperature using a Nucleonix TL reader for γ-ray-irradiated samples.

3 Results and discussions

3.1 Phase analysis

The crystalline structure and phase purity of the synthesized $MgGa_2O_4$:Er^{3+} nanoparticles with varying Er^{3+} concentrations (0–9 mol%) were investigated using PXRD, and the corresponding diffraction patterns are presented in Fig. 1(a). The

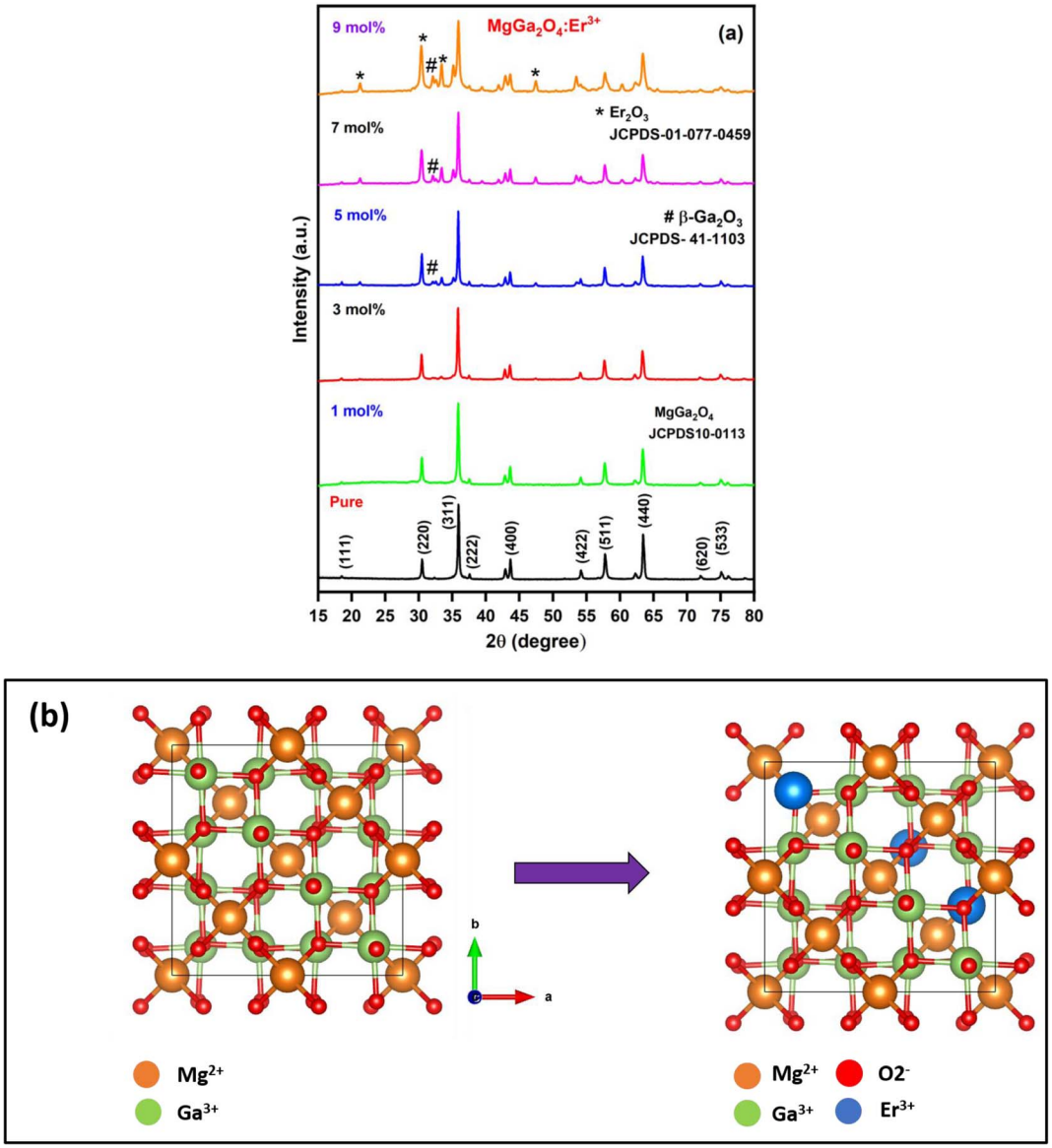

Fig. 1 (a) PXRD patterns of pure $MgGa_2O_4$ and $MgGa_2O_4$:Er^{3+}(1–9 mol%) nanoparticles. (b) Schematic representation of the $MgGa_2O_4$ spinel structure before and after Er^{3+} substitution at Ga^{3+} sites.

undoped $MgGa_2O_4$ sample shows distinct and sharp peaks that match well with the standard cubic spinel structure of $MgGa_2O_4$ (JCPDS Card no. 10-0113).[39,40] The major diffraction peaks observed at 2θ values around 31.3°, 36.9°, 44.8°, 55.6°, 59.3°, 65.2°, and 74.5° correspond to the (220), (311), (400), (422), (511), (440), and (533) crystal planes, respectively. The presence of these peaks without any additional reflections confirms the formation of a single-phase spinel structure with a high degree of crystallinity and structural homogeneity. $MgGa_2O_4$ is a normal spinel material where Mg^{2+} ions occupy the tetrahedral (A) sites and Ga^{3+} ions occupy the octahedral (B) sites in the $Fd\bar{3}m$ space group. When Er^{3+} ions are introduced into the lattice, they are expected to replace Ga^{3+} ions at the octahedral sites due to the close match in charge and comparable ionic radii (Ga^{3+} = 0.62 Å; Er^{3+} = 0.89 Å). This substitution slightly distorts the local crystal field but does not cause a significant change in the overall structure, especially at low doping levels (1–3 mol%).

To visually represent the effect of Er^{3+} substitution, a schematic diagram as shown in (Fig. 1(b)), it depicts the undoped $MgGa_2O_4$ spinel lattice and the structural modification after Er^{3+} incorporation. In the pristine structure, Mg^{2+} ions occupy tetrahedral (A) sites and Ga^{3+} ions occupy octahedral (B) sites within the $Fd\bar{3}m$ cubic spinel framework. Upon Er^{3+} doping, a fraction of Ga^{3+} ions at the B sites are replaced by larger Er^{3+} ions, inducing local lattice distortion and charge-compensating oxygen vacancies. This visualization aids in understanding how Er^{3+} substitution alters the crystal field and influences structural and optical behavior.

For Er^{3+} doping up to 3 mol%, the XRD patterns remain consistent with the pure $MgGa_2O_4$ phase, showing no extra peaks, which indicates that Er^{3+} ions are uniformly

incorporated into the host lattice without altering the spinel symmetry. The absence of impurity peaks at these concentrations confirms successful substitution and suggests that the solubility limit of Er^{3+} in $MgGa_2O_4$ is not exceeded at this stage. Additionally, the peak intensity slightly decreases, and marginal broadening is noticed, implying the introduction of lattice strain and a minor reduction in crystallite size, which are common effects associated with ionic substitution and lattice distortion.

As the Er^{3+} concentration increases beyond 5 mol%, new weak peaks begin to appear in the diffraction pattern. These additional peaks correspond to the β-Ga_2O_3 phase (marked with #) and are indexed using the JCPDS card no. 41-1103.[41] The presence of β-Ga_2O_3 indicates that excess Er^{3+} doping leads to partial segregation of Ga_2O_3, arising from the inability of the host lattice to accommodate a high concentration of Er^{3+} ions due to size mismatch and charge compensation effects. The substitution of larger Er^{3+} ions generates internal lattice strain, which eventually causes local phase separation as the dopant concentration increases. At higher dopant levels (7 and 9 mol%), additional diffraction peaks are observed at 2θ values corresponding to Er_2O_3 (marked with *), identified from the JCPDS file No. 01-077-0459.[42] The emergence of these peaks confirms the formation of a secondary Er_2O_3 phase, which becomes more pronounced with increasing Er^{3+} content. This secondary phase formation is attributed to the oversaturation of Er^{3+} ions within the host lattice, exceeding its solubility limit, leading to Er_2O_3 precipitation on the particle surfaces or grain boundaries during the high-temperature calcination process.

The gradual changes in the XRD peak intensity and width also reflect the influence of dopant concentration on crystallite size and lattice strain. According to the Debye–Scherrer equation,[43] peak broadening is inversely related to crystallite size, suggesting that increased Er^{3+} incorporation slightly reduces the average crystallite size from 30 to 20 nm. Due to the hindrance of grain growth caused by dopant segregation and the creation of strain fields within the lattice. The average crystallite size (D) was calculated using the Debye–Scherrer formula[44,45]

$$D = \frac{K\lambda}{\beta \cos \theta} \quad (1)$$

where K is the shape factor (taken as 0.9), λ is the X-ray wavelength of Cu-Kα radiation (1.541 Å), β is the full width at half maximum (FWHM) of the most intense (3 1 1) diffraction peak (in radians), and θ is the corresponding Bragg's angle. The calculated crystallite size therefore represents the coherent diffraction domain, which is generally smaller than the actual particle size observed in TEM images. This difference arises because XRD determines the size of defect-free crystalline regions, whereas TEM images show the overall particle, which may consist of multiple crystallites aggregated together. The consistency in nanoscale dimensions across all techniques confirms successful synthesis of nanocrystalline $MgGa_2O_4$:Er^{3+} powders.[46] The estimated crystallite size and corresponding optical bandgap values obtained for pure and Er^{3+}-doped $MgGa_2O_4$ nanoparticles are summarized in Table 1.

Table 1 Estimated crystallite size and band gap values of pure $MgGa_2O_4$ and $MgGa_2O_4$:Er^{3+}(1–9 mol%) nanoparticles

Sample	Average crystallite Size(nm) Debye–Scherrer's method (d)	Band gap (eV)
Pure	30	5.10
1 mol%	27	5.17
3 mol%	25	5.06
5 mol%	24	4.95
7 mol%	21	4.90
9 mol%	20	4.86

Moreover, the slight peak shift toward lower 2θ angles at higher doping levels suggests lattice expansion due to substitution of larger Er^{3+} ions for smaller Ga^{3+} ions. The observed trends clearly indicate that Er^{3+} ions are successfully incorporated into the $MgGa_2O_4$ matrix up to approximately 3 mol%, beyond which phase segregation occurs, leading to the coexistence of secondary β-Ga_2O_3 and Er_2O_3 phases. These structural modifications are crucial because they directly affect the luminescence efficiency and energy transfer processes in the material. The presence of impurity phases at higher dopant concentrations introduce non-radiative recombination centers, which quench emission intensity.[47]

The optical characteristics of pure and Er^{3+} doped $MgGa_2O_4$ nanoparticles were investigated using UV-visible diffuse reflectance spectroscopy (DRS),[48] and the corresponding spectra are presented in Fig. 2(a). The DRS profiles show strong reflectance in the visible and near-UV regions (200–800 nm), characteristic of wide-band-gap oxide semiconductors. The pure $MgGa_2O_4$ sample exhibits a steep absorption edge near 240–250 nm, consistent with intrinsic band-to-band electronic transitions within the $MgGa_2O_4$ lattice. This behavior corresponds to the charge transfer between $O^{2-} \rightarrow Ga^{3+}$ ions in the tetrahedral and octahedral sites of the spinel structure. Upon Er^{3+} incorporation (1–9 mol%), a noticeable change in reflectance intensity and the position of the absorption edge is observed. At low doping levels (1 mol%), a slight blue shift of the absorption edge occurs, indicating a minor widening of the optical band gap. This is attributed to the Burstein–Moss effect, which arises from the filling of lower energy states in the conduction band by excess electrons introduced by dopant ions. Consequently, optical transitions require higher photon energy, resulting in an apparent increase in the band gap energy.

This initial widening of the band gap observed at 1 mol% Er^{3+} is attributed to the Burstein–Moss effect, wherein the incorporation of a small amount of Er^{3+} ions introduces additional charge carriers that occupy the lower energy states in the conduction band. This upward shift of the Fermi level effectively increases the optical transition threshold, resulting in a slight apparent widening of the band gap. At such low dopant levels, the number of charge carriers is insufficient to induce significant lattice strain or defect formation, and hence the Burstein–Moss effect dominates. However, with further increase in Er^{3+} concentration, lattice distortion, defect generation, and the formation of Er^{3+}–O–Ga defect complexes and

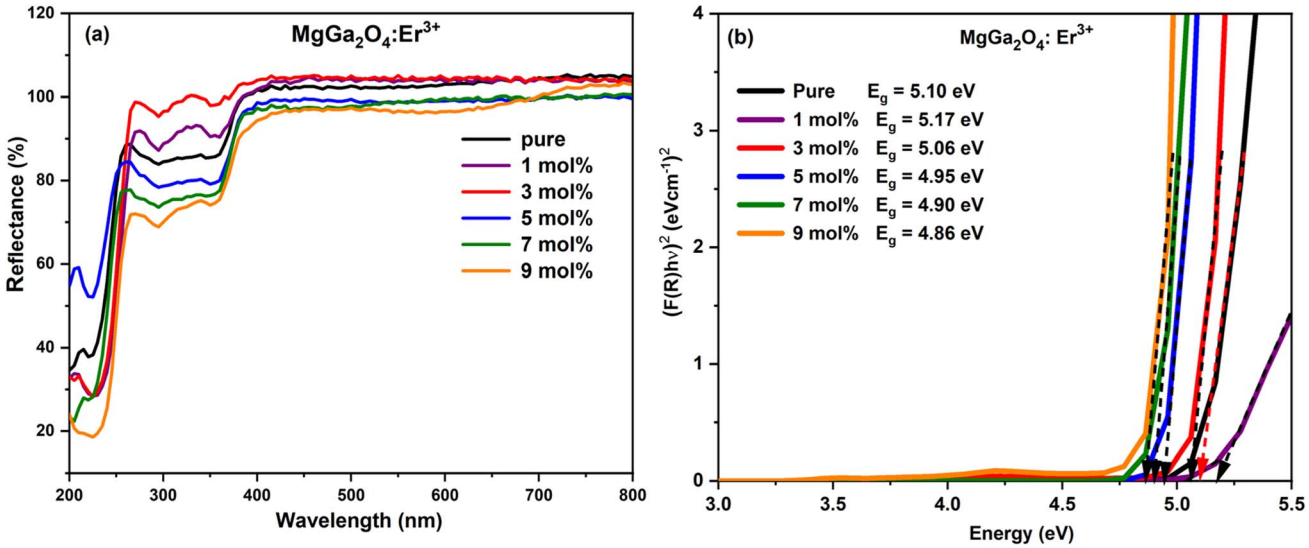

Fig. 2 (a) UV-vis diffuse reflectance spectra and (b) Tauc plot for pure $MgGa_2O_4$ and $MgGa_2O_4$:Er^{3+} (1–9 mol%) nanoparticles.

oxygen vacancies become more pronounced. These defect states create localized energy levels within the band gap, leading to band tailing and the observed red shift (band-gap narrowing) at higher doping levels. As the Er^{3+} concentration increases beyond 3 mol%, the absorption edge gradually shifts toward longer wavelengths (red shift), accompanied by a decrease in reflectance intensity. This behavior suggests a narrowing of the band gap, likely caused by increased dopant-induced lattice disorder, defect generation, and the formation of impurity energy levels within the forbidden gap. These defects, such as oxygen vacancies and Er–O–Ga coordination distortions, act as shallow donor or acceptor levels, facilitating sub-band-gap transitions and reducing the optical energy gap. It should be noted that the apparent contradiction between the optical and morphological analyses arises from the different nature of defects probed by each technique. The optical band-gap reduction at 3 mol% Er^{3+} results from localized electronic defect states (Er^{3+} associated oxygen-vacancy and Er–O–Ga complexes) that alter the electronic structure of the lattice. In contrast, the SEM micrographs (Fig. 4) reveal smoother and more uniform grains, indicating reduced surface and grain-boundary defects. Therefore, although the crystallinity improves at 3 mol% Er^{3+}, the slight band-gap narrowing is governed by electronic defect formation rather than by an increase in structural disorder.

Fig. 2(b) presents the Tauc plots representing $(F(R)h\nu)^2$ *versus* photon energy ($h\nu$),[49] where the linear region of each curve was extrapolated to the energy axis to determine the optical band gap (E_g) for direct allowed transitions. The obtained E_g values are 5.10, 5.17, 5.06, 4.95, 4.90 and 4.86 eV for pure and 1, 3, 5, 7, 9 respectively. These results confirm the initial slight widening of the band gap at lower doping, followed by a systematic narrowing at higher Er^{3+} concentrations. The observed band-gap modulation is due to the combined effect of lattice strain, local field variations, and dopant-induced defect states. The initial increase at 1 mol% Er^{3+} results from substitutional incorporation of Er^{3+} ions at Ga^{3+} sites, which slightly reduces carrier-phonon scattering and stabilizes the crystal lattice. However, further doping introduces structural distortions and charge imbalance due to the larger ionic radius of Er^{3+} compared to Ga^{3+}, leading to lattice relaxation and defect formation. These localized defect states near the conduction and valence bands enhance electron–hole recombination probability and reduce the effective band gap.

Additionally, the presence of Er^{3+} ions introduces localized 4f electronic states, which can couple with the host lattice electronic states, affecting optical absorption characteristics. The gradual decrease in E_g with higher doping suggests that the energy levels associated with Er^{3+} 4f–5d transitions overlap with the conduction band edge, thus reducing the effective optical threshold. The consistent decrease in reflectance with higher Er^{3+} doping also supports the increase in light absorption, beneficial for enhancing the material's luminescence efficiency under visible and near-UV excitation. The high reflectance in the visible region further confirms the suitability of $MgGa_2O_4$:Er^{3+} nanoparticles for optical and phosphor-based applications, especially in white-light-emitting diodes (WLEDs).[50,51]

FTIR spectra of pure and Er^{3+}-doped $MgGa_2O_4$ nanoparticles with varying Er^{3+} concentrations (3 & 7 mol%) are shown in Fig. (3). The spectra were recorded in the range of 4000–400 cm^{-1} to analyze the functional groups, bonding characteristics, and structural integrity of the synthesized materials. The overall spectral profile confirms the formation of the spinel structure and the successful incorporation of Er^{3+} ions into the $MgGa_2O_4$ lattice without introducing new impurity phases. A broad absorption band centered around 3340 cm^{-1} is observed in all samples and is attributed to the O–H stretching vibrations of adsorbed water molecules or surface hydroxyl groups. This indicates the presence of physically adsorbed moisture due to the high surface area of the nanosized powders. The weak bands appearing near 2968 cm^{-1} and 2874 cm^{-1} correspond to C–H stretching vibrations, which are likely residual organic traces from the urea fuel used in the combustion synthesis process. Their reduced intensity in doped samples suggests

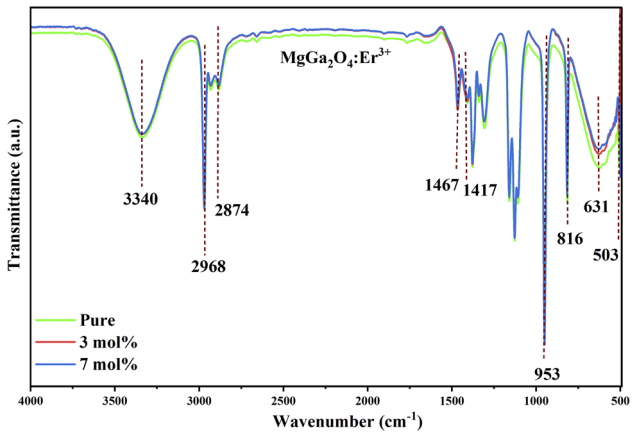

Fig. 3 FTIR spectra of pure $MgGa_2O_4$ and $MgGa_2O_4$:Er^{3+} (1 and 7 mol%) nanoparticles.

effective decomposition of organic species during calcination at 1000 °C.[52,53]

The absorption bands observed at 1467 cm^{-1} and 1417 cm^{-1} are assigned to asymmetric and symmetric stretching vibrations of the carbonate (CO_3^{2-}) groups, which may form due to atmospheric CO_2 adsorption on the sample surface. The slight broadening and reduced intensity of these bands with higher Er^{3+} content indicate better crystallinity and fewer surface carbonates after doping and high-temperature treatment. The most prominent features of the spectra lie in the lower wavenumber region (below 1000 cm^{-1}), which is characteristic of metal–oxygen (M–O) lattice vibrations in spinel oxides. The strong absorption bands at 8953 cm^{-1} and 816 cm^{-1} correspond to the stretching vibrations of Ga–O bonds in tetrahedral and octahedral sites, respectively. These vibrations confirm the spinel framework of $MgGa_2O_4$. The additional absorption peaks located at 633 cm^{-1} and 503 cm^{-1} are attributed to Mg–O stretching and bending modes, respectively, within the spinel lattice. The appearance and stability of these bands across all samples confirm the structural integrity of the $MgGa_2O_4$ phase, even after Er^{3+} substitution.

Notably, as the Er^{3+} doping concentration increases, slight shifts and intensity variations are observed in the M–O bands, particularly around 816 cm^{-1} and 503 cm^{-1}. These shifts arise from lattice distortions caused by substitution of Ga^{3+} (0.62 Å) by larger Er^{3+} ions (0.89 Å), which modifies the local bonding environment and affects Ga–O–Mg vibrational coupling. The minor changes also suggest successful partial substitution of Er^{3+} ions in the octahedral sites of the $MgGa_2O_4$ lattice rather than forming separate oxide phases, consistent with the XRD results. At higher Er^{3+} concentrations (≥7 mol%), no new bands are detected, but slight broadening in the Ga–O and Mg–O vibrational regions is noticed. This is attributed to increased structural disorder and local strain arising from dopant-induced distortion, oxygen vacancy formation, or defect clustering at the lattice boundaries. These localized defects can influence optical and luminescent behaviors by introducing intermediate energy states, which are advantageous for photonic applications.

3.2 Morphology analysis

The pure $MgGa_2O_4$ sample (Fig. 4) exhibits an agglomerated morphology with irregularly shaped grains forming a porous network. This porous nature results from the rapid gas evolution during the combustion synthesis process, which promotes the formation of loosely connected crystallites. The individual nanoparticles appear fused, suggesting localized sintering due to the exothermic nature of the reaction. Upon doping with 1 mol% Er^{3+}, the microstructure shows a more compact and uniform morphology with smaller and nearly spherical particles. The reduction in particle size is attributed to the substitution of Er^{3+} ions into the $MgGa_2O_4$ lattice, which introduces lattice strain and inhibits grain coalescence during calcination. This controlled particle growth leads to improved surface uniformity and enhanced crystallinity, consistent with XRD results. At 3 mol% doping, the surface becomes smoother, and the particles exhibit moderate agglomeration with well-defined grain boundaries. The nanoparticles are more interconnected, suggesting enhanced densification and grain growth due to increased thermal diffusion during calcination. This morphology supports effective energy transfer in luminescence applications, as it minimizes surface defects that often act as quenching centers.

The 5 mol% Er^{3+}-doped sample maintains a similar structure, though the grains appear slightly larger and more closely packed. This suggests the onset of particle coarsening caused by higher dopant-induced lattice distortion and grain boundary migration. However, the overall surface remains homogeneous, confirming stable growth dynamics up to this concentration. A distinct change is observed at 7 mol% Er^{3+} doping, where the surface becomes rougher and displays irregularly shaped grains with voids. The grain boundaries are less distinct, indicating partial melting or local stress accumulation during synthesis. This microstructural evolution implies that the solubility limit of Er^{3+} in the $MgGa_2O_4$ lattice is being approached, resulting in partial segregation and local non-uniformities. At the highest doping level (9 mol%), the morphology significantly changes, showing well-separated spherical nanoparticles and noticeable phase segregation. The surface appears granular, and the particle distribution becomes more discrete, consistent with the XRD evidence of secondary phase formation (Er_2O_3 and β-Ga_2O_3). The reduced connectivity between grains and formation of smaller spherical clusters suggest localized nucleation of Er-rich regions, indicating dopant oversaturation within the host matrix. Overall, the SEM analysis reveals a clear evolution of morphology with increasing Er^{3+} content: from irregular agglomerates in the pure sample to fine spherical grains at lower doping, and finally to segregated particles at higher doping levels. This progression demonstrates that controlled Er^{3+} incorporation up to 3–5 mol% promotes uniform nanostructure formation, while excessive doping (≥7 mol%) leads to lattice strain, phase separation, and morphological degradation.

The EDX spectra corresponding to pure and Er^{3+}-doped $MgGa_2O_4$ nanoparticles (Fig. 4(a–f)) confirm the presence of Mg, Ga, and O as the primary constituent elements, validating the

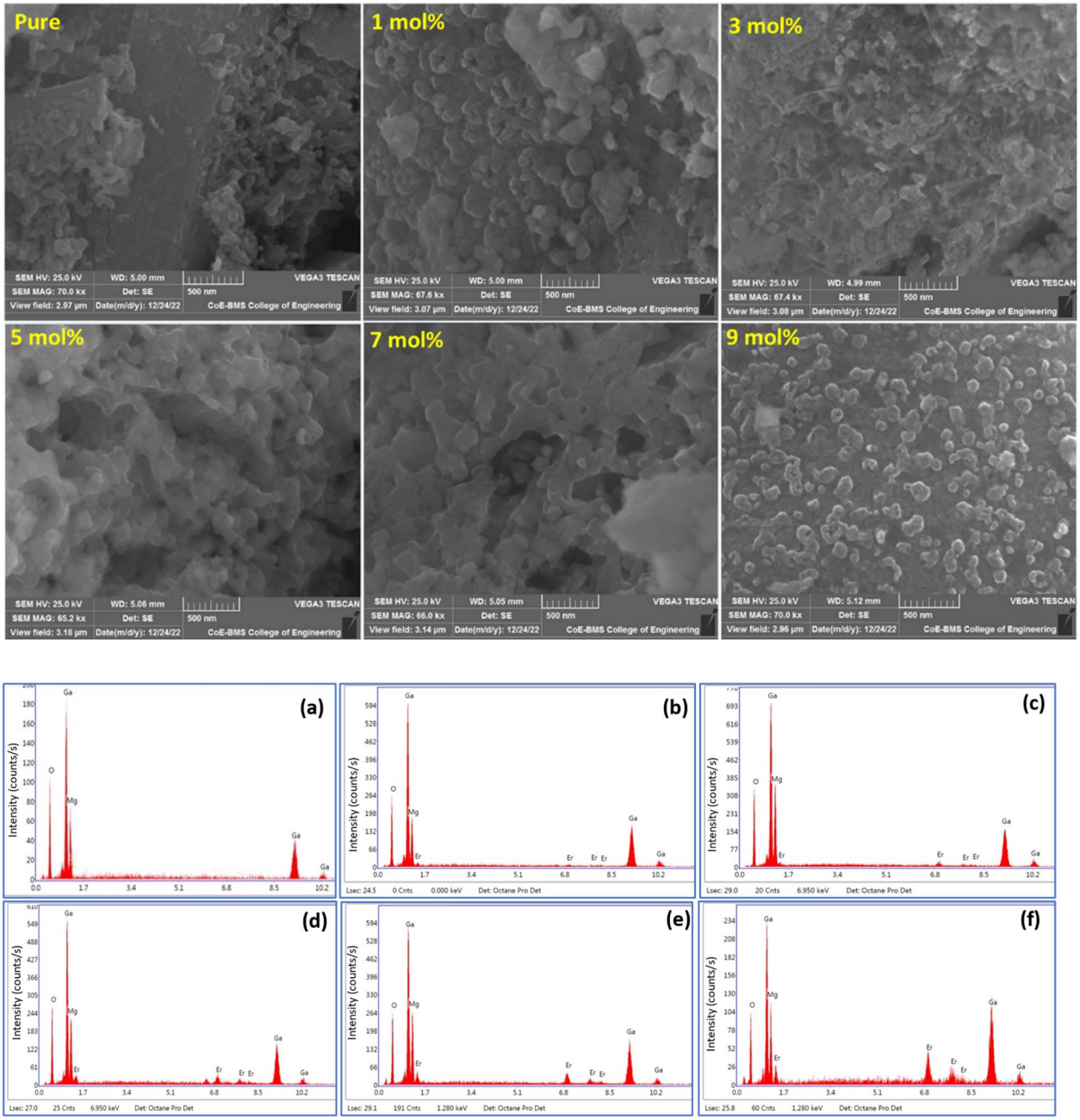

Fig. 4 SEM images of pure $MgGa_2O_4$ and $MgGa_2O_4$:Er^{3+} (1–9 mol%) nanoparticles, (a–f) shows the EDAX spectrum of pure and $MgGa_2O_4$:Er^{3+} (1–9 mol%) nanoparticles.

expected stoichiometry of the spinel matrix. For doped samples, additional peaks corresponding to Er are distinctly observed, confirming successful incorporation of Er^{3+} ions into the host lattice. In the pure sample (Fig. 4(a)), the elemental peaks of Mg (around 1.25 keV), Ga (9.2–10.3 keV), and O (0.52 keV) are clearly visible, confirming the formation of stoichiometric $MgGa_2O_4$. Upon doping with 1 mol% Er^{3+} (Fig. 4(b)), a weak Er signal appears near 6.8 keV, indicating that trace levels of the dopant are effectively incorporated without altering the base composition.

The Er peak intensity systematically increases with higher doping concentrations (Fig. 4c–f), validating the progressive inclusion of Er^{3+} ions within the material. The quantitative EDX results, summarized in Table 2 in SI, show that the atomic percentages of Mg, Ga, and O remain close to the stoichiometric ratio, with a consistent increase in Er content proportional to the nominal doping level. This consistency confirms homogeneous dispersion of Er^{3+} ions across the surface without significant compositional deviation up to 5 mol%. However, at higher concentrations (≥7 mol%), slight fluctuations in the Mg and Ga peaks are observed, consistent with partial segregation of Er-rich and Ga-deficient regions detected in XRD analysis. Importantly, no impurity elements such as carbon or nitrogen are detected in the EDX spectra, confirming the complete

Table 2 Elemental composition of pure $MgGa_2O_4$ and $MgGa_2O_4$:Er^{3+} (1–9 mol%)

	Element	Weight %	Atomic %
$MgGa_2O_4$	O K	28.05	54.15
	Ga L	50.02	21.49
	Mg K	21.93	21.49
$MgGa_2O_4$:Er 1%	O K	27.68	47.65
	Ga L	50.70	28.08
	Mg K	21.29	23.91
	Er L	1.78	0.36
$MgGa_2O_4$:Er 3%	O K	23.09	46.27
	Ga L	50.87	23.40
	Mg K	22.49	29.66
	Er L	3.55	0.68
$MgGa_2O_4$:Er 5%	O K	23.19	48.25
	Ga L	48.93	23.36
	Mg K	19.53	26.73
	Er L	8.36	1.66
$MgGa_2O_4$:Er 7%	O K	22.93	47.79
	Ga L	48.30	23.10
	Mg K	19.94	27.35
	Er L	8.84	1.76
$MgGa_2O_4$:Er 9%	O K	16.72	43.35
	Mg K	13.10	22.35
	Er L	21.53	5.34
	Ga K	48.66	28.96

removal of residual fuel components from the combustion process. The elemental uniformity confirmed by EDAX spectra (Fig. 4(a–f)), together with the single-phase XRD patterns, provides sufficient evidence for homogeneous dopant incorporation, eliminating the need for separate elemental mapping in the present study. This purity supports the successful synthesis of high-quality Er^{3+} doped $MgGa_2O_4$ nanoparticles.

3.3 HRTEM analysis

Fig. 5(a–e) illustrates the high-resolution transmission electron microscopy (HRTEM) images, selected area electron diffraction (SAED) pattern, and particle size distribution of the $MgGa_2O_4$:Er^{3+} (3 mol%) nanoparticles. These analysis were carried out to investigate the particle morphology, crystallinity, and structural order at the nanoscale. The low-magnification HRTEM image (Fig. 5(a)) reveals with irregular boundaries, typical of combustion-synthesized oxides. The particles exhibit nearly spherical shapes with moderate clustering, which results from rapid nucleation and limited growth during the exothermic combustion reaction. The average particle size appears to be in the nanometric range, corroborating SEM observations. A closer inspection of the high-magnification image (Fig. 5(b)) shows well-resolved lattice fringes, confirming the high crystallinity of the sample. The uniform lattice arrangement suggests that the Er^{3+} ions are successfully incorporated into the $MgGa_2O_4$ host lattice without disrupting its structural periodicity. The clear visibility of lattice planes indicates the absence of significant amorphous regions or grain boundary dislocations.

Fig. 5(c) displays the lattice fringe spacing, where the measured interplanar distance (d) is approximately 0.298 nm, corresponding to the (220) crystal plane of the cubic spinel $MgGa_2O_4$ structure (JCPDS No. 10-0113). This value aligns closely with the XRD-derived data, confirming the preservation of the spinel phase and validating that Er^{3+} substitution does not alter the fundamental crystallographic framework.

The SAED pattern shown in Fig. 5(d) exhibits distinct and concentric diffraction rings indexed to the (220), (311), (222), (400), (422), (511), and (440) planes of cubic $MgGa_2O_4$. The presence of sharp, well-defined rings indicates a polycrystalline nature with nanocrystalline domains uniformly oriented throughout the sample. The absence of additional diffraction spots or diffuse halos further confirms the single-phase crystalline nature of the Er^{3+}-doped $MgGa_2O_4$. Fig. 5(e) presents the particle size distribution histogram, which was obtained from several HRTEM micrographs. The particle size distribution follows a Gaussian trend with an average particle size of approximately 51 nm. This size agrees well with the crystallite size calculated using the Scherrer equation from XRD results, confirming that the nanoparticles are predominantly single crystalline. The relatively narrow distribution implies homogeneous growth and minimal particle agglomeration, validating the effectiveness of the solution combustion synthesis (SCS) process in producing uniform nanostructures.

3.4 Analysis of luminescence properties

Fig. 6(a) shows the excitation spectra of $MgGa_2O_4$:Er^{3+} nanoparticles recorded at an emission wavelength of 551 nm, the photoluminescence behavior of undoped $MgGa_2O_4$ has been previously reported by our group Jyothi *et al.*,[54] showing only weak intrinsic emission in the near-UV region. Hence, the present discussion focuses on the enhancement and spectral evolution induced by Er^{3+} doping. Corresponding to the green emission band of Er^{3+}. All samples exhibit a strong excitation peak centered around 381 nm, which originates from the $^4I_{15/2} \rightarrow {}^4G_{11/2}$ electronic transition of Er^{3+} ions. This peak confirms the efficient excitation of Er^{3+} ions through direct f–f transitions within the host lattice. The excitation intensity increases with Er^{3+} concentration up to 3 mol%, beyond which it gradually decreases. The enhancement up to this concentration indicates improved energy transfer from the host lattice to Er^{3+} ions due to optimized dopant–host interaction and minimal nonradiative losses.[55] At higher concentrations (≥5 mol%), the reduction in intensity is attributed to concentration quenching, a common phenomenon caused by nonradiative energy migration between adjacent Er^{3+} ions through cross-relaxation or dipole–dipole interactions.[56]

This behavior confirms that the optimum doping concentration for efficient excitation in $MgGa_2O_4$:Er^{3+} is approximately 3 mol%, beyond which the probability of nonradiative transitions increases due to excessive Er^{3+} clustering and defect formation.[57,58]

The corresponding PL emission spectra under 381 nm excitation are presented in Fig. 6(b). All samples display three prominent emission bands centered around 523, 551, and 625 nm, corresponding to the $^2H_{11/2} \rightarrow {}^4I_{15/2}$, $^4S_{3/2} \rightarrow {}^4I_{15/2}$, and $^4F_{9/2} \rightarrow {}^4I_{15/2}$ transitions of Er^{3+} ions, respectively. The

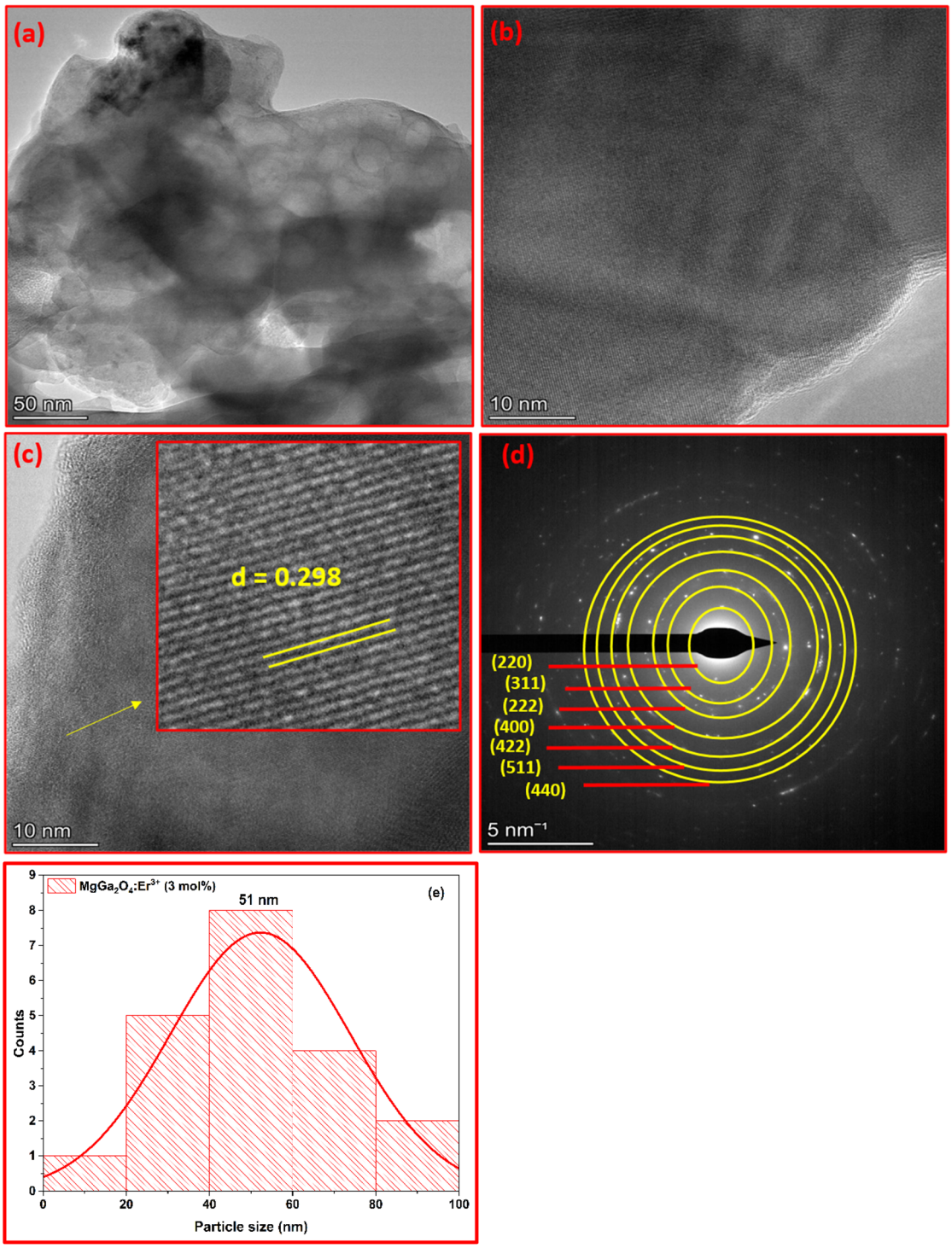

Fig. 5 HRTEM images and SAED patterns of $MgGa_2O_4:Er^{3+}$ 3 mol% nanoparticles: (a and b) HRTEM images of $MgGa_2O_4:Er^{3+}$ 3 mol%, (c) lattice fringes showing an interplanar distance (d) SAED pattern of $MgGa_2O_4:Er^{3+}$ 3 mol%, (e) particle size distribution of $MgGa_2O_4:Er^{3+}$ 3 mol% nanoparticles.

dominant emission peak at 551 nm (green) arises from the $^4S_{3/2} \rightarrow {}^4I_{15/2}$ transition, dominating the characteristic green luminescence. The intensity of these emission bands follows the same trend as the excitation spectra, peaking at 3 mol% Er^{3+} concentration. The enhancement up to this concentration is due to efficient radiative recombination facilitated by the crystalline environment of the $MgGa_2O_4$ host. Beyond 3 mol%, the luminescence intensity decreases because of cross-relaxation processes, where excited Er^{3+} ions transfer energy to neighboring ions, leading to nonradiative relaxation. The well-resolved emission peaks demonstrate that Er^{3+} ions are successfully integrated into the lattice rather than forming

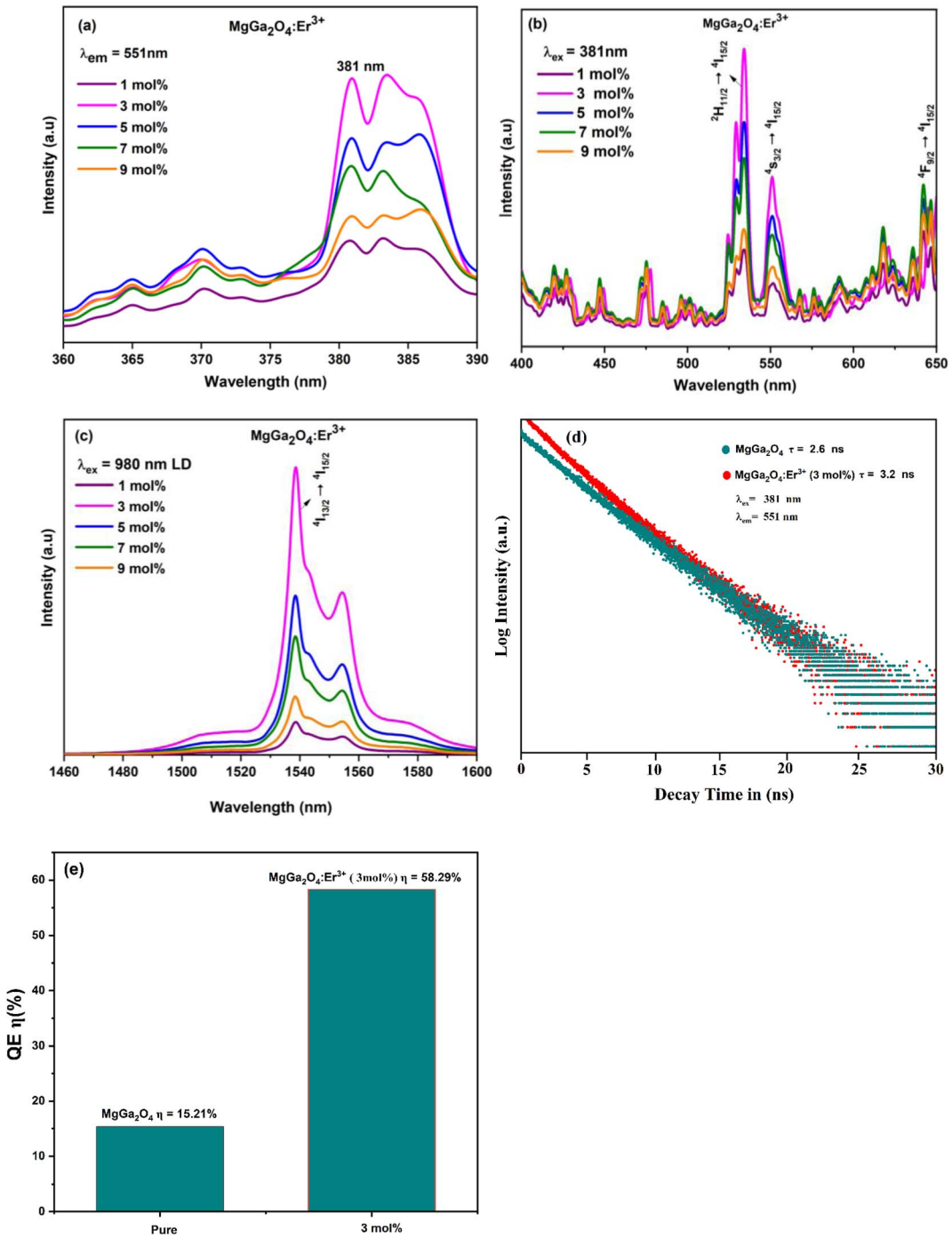

Fig. 6 (a and b) Visible excitation $MgGa_2O_4:Er^{3+}$ (1–9 mol%) and emission spectra of $MgGa_2O_4:Er^{3+}$ (1–9 mol%) nanoparticles. (c) NIR emission spectra under 980 nm LD, (d) photoluminescence (PL) decay curves of pure $MgGa_2O_4$ and $MgGa_2O_4:Er^{3+}$ (1–9 mol%) nanoparticles and (e) variation in QE (η) of pure $MgGa_2O_4$ and $MgGa_2O_4:Er^{3+}$ (3 mol%) nanoparticles.

separate Er_2O_3 clusters. The host matrix's wide band gap (~5 eV) minimizes thermal quenching, enabling stable emission even at higher excitation powers. This makes $MgGa_2O_4:Er^{3+}$ a promising phosphor for visible light-emitting diode (WLED) applications.

Fig. 6(c) presents the NIR PL emission spectra of $MgGa_2O_4:Er^{3+}$ nanoparticles in NIR region under 980 nm laser diode (LD) excitation. A strong emission peak centered at 1540 nm is observed, corresponding to the $^4I_{13/2} \rightarrow {}^4I_{15/2}$ transition of Er^{3+} ions. This NIR emission is particularly important for telecommunication (1.5 μm window) and biomedical imaging applications. The intensity variation follows the same trend as in visible PL spectra, with maximum emission at 3 mol% Er^{3+}. This indicates optimal population of the $^4I_{13/2}$ excited state through efficient ground-state absorption and energy transfer processes. The decline in emission intensity beyond this concentration

again results from concentration quenching and energy back-transfer to the lattice. The well-defined NIR emission demonstrates that the $MgGa_2O_4$ matrix provides a low-phonon-energy environment (~700 cm^{-1}), reducing nonradiative multiphonon relaxation and enhancing radiative efficiency. Thus, $MgGa_2O_4$:Er^{3+} acts as a dual-emitting phosphor suitable for both visible and NIR photonic applications.[59,60]

Fig. 6(d) shows the PL decay curves of pure and $MgGa_2O_4$:Er^{3+} (3 mol%) nanoparticles. To determine the decay lifetimes,[61] we have applied an exponential decay model, where the luminescence intensity, $I(t)$, is plotted as a function of time t, typically follows an exponential decay function.[62]

$$I(t) = I\, e^{-t/\tau} \quad (2)$$

where $I(t)$ is the luminescence intensity at time t, I is the initial luminescence intensity at, "$t = 0$, where τ is the decay lifetime.[63,64] This decay function characterizes the persistence of luminescence in a material, with longer decay times indicating a slower recombination process and a more persistent luminescent response. The average lifetime for pure $MgGa_2O_4$ is 2.6 ns, whereas for the 3 mol% Er^{3+}-doped sample, it increases to 3.2 ns. The longer lifetime in the doped sample reflects reduced nonradiative pathways and efficient energy confinement in the Er^{3+} 4f shell. The increase in τ also indicates effective suppression of defect-related recombination due to the Er^{3+} ions acting as luminescent centers. At higher dopant levels, the lifetime tends to shorten (not shown here) due to cross-relaxation among Er^{3+} ions and defect-assisted quenching, confirming the critical doping threshold at 3 mol%.

Fig. 6(e) shows the variation of QE (η) in pure and $MgGa_2O_4$:Er^{3+} (3 mol%) nanoparticles. The quantum yield (QY) calculations for each sample were performed using an integrating sphere setup attached to a spectrophotometer, which allowed for precise measurement of absorbed and emitted photon intensities. The quantum yield (Φ, was calculated based on the ratio of emitted to absorbed photons using the formula.[65]

$$\varphi = \frac{\text{Number of photons emitted}}{\text{Number of photons absorbed}} \quad (3)$$

where φ represents the fraction of absorbed photons that are converted into emitted photons.[66] The pure sample exhibits a QE of 15.21%, whereas the doped sample achieves a significantly higher QE of 58.29%. This nearly fourfold enhancement arises from the introduction of efficient Er^{3+} luminescent centers that convert absorbed photons into visible and NIR emissions with minimal losses. The improvement in QE correlates with optimized crystallinity, reduced defect density, and the suitable electronic environment provided by the $MgGa_2O_4$ host. The cubic spinel structure offers strong crystal field interactions, promoting f–f electronic transitions within Er^{3+} without significant phonon coupling, thereby enhancing radiative recombination probability. The overall luminescence process under UV (381 nm) or NIR (980 nm) excitation. Although a reduction in structural defect density is expected for the 1, 5, 7, and 9 mol% Er^{3+} sample, its comparatively weaker PL intensity (Fig. 6(b)) indicates reduced host–dopant energy transfer efficiency. As a result, the measured quantum yield for the optimized 3 mol% composition was selected to represent the most efficient luminescent performance, while the 1,5,7 and 9 mol% sample were not further evaluated due to its low emission intensity. Electrons in Er^{3+} ions are promoted from the ground state ($^4I_{15/2}$) to higher excited states ($^4G_{11/2}$ or $^4I_{11/2}$). Nonradiative relaxation to intermediate levels ($^2H_{11/2}$, $^4S_{3/2}$, $^4F_{9/2}$, and $^4I_{13/2}$) leads to radiative transitions that produce visible green (551 nm) and NIR (1540 nm) emissions. The $MgGa_2O_4$ host, with its low phonon energy and high band gap, minimizes nonradiative decay, thus enhancing emission intensity and stability. At optimal Er^{3+} concentration (3 mol%), efficient energy transfer occurs between the host and dopant ions. However, beyond this level, energy migration among Er^{3+} ions increase, causing nonradiative losses through cross-relaxation and back-transfer to lattice vibrations, reducing both intensity and QE. These results confirm that $MgGa_2O_4$:Er^{3+} nanoparticles, particularly at 3 mol% doping, exhibit strong and efficient visible-NIR luminescence, making them excellent candidates for WLEDs, photonic amplifiers, and optical sensor applications.[67–69]

Fig. 7 illustrates the Commission Internationale de l'Eclairage (CIE 1931) chromaticity diagram and correlated color temperature (CCT),[70,71] distribution for $MgGa_2O_4$:Er^{3+} nanoparticles doped with different Er^{3+} concentrations (1–9 mol%). The diagram provides a graphical representation of the emission color coordinates (x, y), which define the visual color output of the phosphor material, while the CCT values describe the perceived "warmth" or "coolness" of the emitted light. The CIE coordinates for all samples fall in the green-yellow region of the visible spectrum, confirming that the luminescence is primarily dominated by Er^{3+} 4f transitions, particularly $^4S_{3/2} \rightarrow {}^4I_{15/2}$ and $^2H_{11/2} \rightarrow {}^4I_{15/2}$, which emit strong green light near 551 nm. The specific chromaticity coordinates (x, y) obtained for various Er^{3+} concentrations are tabulated in Table 3 and

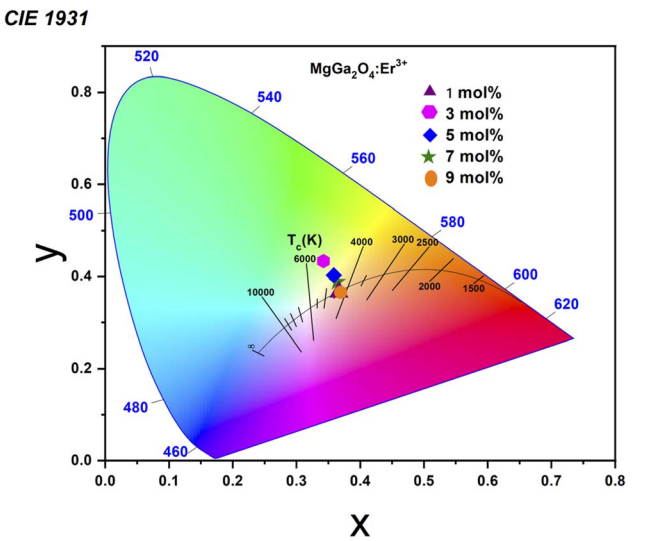

Fig. 7 CIE & CCT diagram of $MgGa_2O_4$:Er^{3+}(1–9 mol%) nanoparticles.

Table 3 Photometric values of $MgGa_2O_4:Er^{3+}$ (1–9 mol%) nanoparticles

$MgGa_2O_4:Er^{3+}$ (concentration)	x	y	CCT (K)	CRI
1 mol%	0.341	0.434	4268	73
3 mol%	0.368	0.365	5291	90
5 mol%	0.363	0.388	4554	88
7 mol%	0.365	0.366	4353	87
9 mol%	0.357	0.402	4770	83

show only minor shifts, indicating good color stability of the $MgGa_2O_4:Er^{3+}$ system.

At 1 mol% Er^{3+}, the emission point lies slightly toward the yellowish-green region, indicating a balance between green and weak red emissions from the $^4F_{9/2} \rightarrow {}^4I_{15/2}$ transition. As the Er^{3+} concentration increases to 3 mol%, the chromaticity coordinates move closer to the pure green region, corresponding to enhanced $^4S_{3/2} \rightarrow {}^4I_{15/2}$ emission intensity. This shift results from efficient energy transfer and reduced nonradiative decay at the optimal dopant concentration. Consequently, the sample exhibits a more saturated green emission suitable for WLED phosphor applications. Beyond 5 mol%, the CIE points slightly shift back toward the yellow–green boundary. This change is due to concentration quenching effects, where increased Er^{3+}–Er^{3+} interactions lead to partial suppression of green emission intensity and enhancement of red emission contributions from the $^4F_{9/2} \rightarrow {}^4I_{15/2}$ transition. Nonetheless, all data points remain within the green-emission region, confirming the dominant luminescent behavior of Er^{3+} ions within the $MgGa_2O_4$ host.

The CCT values, derived from the CIE coordinates using McCamy's empirical relation, are found in the range of approximately 4000–6000 K for all samples. These values correspond to neutral white to cool white light, which is highly desirable for solid-state lighting applications. Specifically, the 3 mol% Er^{3+}-doped sample, located near the central region of the CIE diagram ($x \approx 0.368$, $y \approx 0.365$), exhibits a correlated color temperature of ~5291 K, corresponding to pure cool white emission. This behavior reflects a balance between the green and red emissions, indicating efficient color mixing. The stable CCT values across varying dopant concentrations demonstrate that the emission color of $MgGa_2O_4:Er^{3+}$ is relatively insensitive to minor compositional changes, highlighting its potential reliability in optoelectronic devices.[72,73]

The position of each CIE point on the 1931 diagram further validates that the luminescence color purity remains high, as the coordinates are located near the edge of the green region rather than toward the central white-light zone. This implies minimal spectral broadening and high chromatic stability, both critical for high-performance phosphors in white LED (WLED) and display technologies. The CIE and CCT analyses confirm that $MgGa_2O_4:Er^{3+}$ nanoparticles, particularly at 3 mol% doping, produce stable, high-purity green emission with CCT suitable for energy-efficient WLED and photonic device applications.[74,75]

3.5 Thermoluminescence (TL) analysis

Fig. 8 presents the thermoluminescence (TL),[76] glow curves of pure and Er^{3+}-doped $MgGa_2O_4$ nanoparticles (1–9 mol%) irradiated at a 5 kGy γ-dose.[77] All the samples display a single broad and prominent glow peak in the temperature range of 150–250 °C, confirming the presence of well-defined, thermally stable traps suitable for medium-temperature dosimetric applications. The position of the main glow peak exhibits a slight shift with Er^{3+} concentration 199 °C for pure, 189 °C for 1 mol%, 212 °C for 3 mol%, 201 °C for 5 mol%, 198 °C for 7 mol%, and 201 °C for 9 mol% indicating minor variations in trap depth due to dopant-induced lattice modifications. These small shifts suggest that the nature of trapping centers,[78,79] remains similar, while their population and activation energy,[80] are influenced by the Er^{3+} concentration.

The pure $MgGa_2O_4$ sample shows a relatively weak TL intensity with a peak at 199 °C, corresponding primarily to intrinsic lattice defects such as oxygen vacancies (V_0), magnesium/gallium antisite defects (Ga_mg, MgGa), or interstitials formed during the combustion synthesis process. The introduction of Er^{3+} ions significantly enhances the TL intensity up to 5 mol%, after which it declines. This trend reflects the classical concentration quenching behavior, where an increase in activator content initially increases the number of trapping and recombination centers, followed by nonradiative energy transfer and defect aggregation at higher concentrations. The increase in TL intensity with Er^{3+} doping up to 5 mol% is attributed to the formation of Er^{3+}–V_0 complex traps and Er^{3+}–Ga^+ defect clusters. The substitution of trivalent Er^{3+} ions at Mg^{2+} or Ga^{3+} lattice sites introduce local charge imbalance, compensated by the creation of oxygen vacancies or antisite defects. These defect complexes act as efficient electron or hole traps, facilitating charge carrier storage during γ-irradiation and their subsequent release upon thermal stimulation. The shift of the main glow peak from 189 °C (1 mol%) to 212 °C (3 mol%) indicates a transition from shallow to moderately

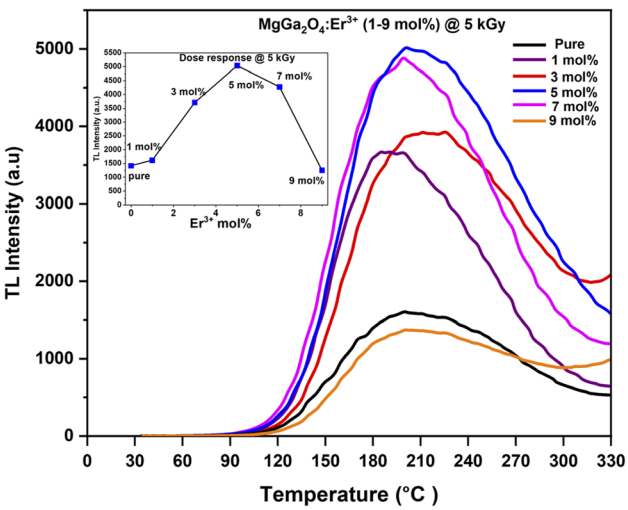

Fig. 8 Thermoluminescence (TL) glow curves of pure $MgGa_2O_4$ and $MgGa_2O_4:Er^{3+}$ (1–9 mol%) nanoparticles irradiated at 5 kGy.

deep traps as Er^{3+} concentration increases, which enhances charge retention and TL efficiency. The 5 mol% Er^{3+} sample exhibits the highest TL intensity with a glow peak centered at 201 °C, confirming optimal trap depth (~1.0 eV) and balanced trap–recombination dynamics. Beyond this concentration (7 and 9 mol%), the TL peak temperature stabilizes near 200 °C, but the intensity decreases sharply, confirming the onset of quenching.

The reduction in TL intensity beyond 5 mol% can be attributed to nonradiative recombination and defect saturation, where excess Er^{3+} ions lead to clustering or the formation of non-emissive Er_2O_3 secondary phases, as evidenced by XRD. These clusters distort the local crystal field, facilitating dipole–dipole energy transfer and suppressing radiative recombination. The inset of Fig. 8 illustrates the variation in TL intensity with Er^{3+} concentration at a fixed dose of 5 kGy. The nearly Gaussian profile, peaking at 5 mol%, clearly identifies the optimal dopant level for maximum TL sensitivity. The TL glow peak position correlates with the thermal stability of traps, which can be approximated from the activation energy using empirical relations. The nearly constant peak temperature (~200 °C) across samples indicates that all Er^{3+} concentrations generate medium-depth traps, ideal for retaining charge carriers at ambient conditions and releasing them only upon heating. The presence of a single, well-resolved glow peak further confirms the dominance of a specific class of traps likely Er^{3+}-associated oxygen vacancies rather than multiple overlapping shallow traps. Upon γ-irradiation, high-energy photons excite electrons from the valence band or Er^{3+} 4f levels to the conduction band, leaving behind holes. Some electrons are captured at defect-associated traps (V_0, Er^{3+}–V_0, or Er^{3+}–Ga^+ complexes), while holes localize at adjacent oxygen sites or Er^{3+} levels. Upon heating, trapped electrons are thermally released and recombine radiatively with holes at Er^{3+} centers, resulting in photon emission corresponding to the $^4S_{3/2} \rightarrow {}^4I_{15/2}$ transition. The trap depth (~0.9–1.2 eV) inferred from the peak temperature supports their classification as medium-deep traps, capable of maintaining TL stability over time. Although no direct experimental verification *via* XPS or EPR was performed, the role of oxygen vacancies and Er^{3+}-defect complexes is strongly supported by the observed TL characteristics, peak positions, and comparative literature on rare-earth-doped spinel systems. In $MgGa_2O_4$, oxygen vacancies are thermodynamically favorable and act as efficient electron traps. The incorporation of Er^{3+} enhances their formation and stabilization, while the associated lattice strain adjusts the local potential well depth, improving charge retention. The consistency of glow peak temperature around 200 °C across dopant concentrations confirms that Er^{3+} primarily modulates trap density rather than creating new trap species.

Fig. 9 displays the thermoluminescence (TL) glow curves of the optimized $MgGa_2O_4$:Er^{3+} (5 mol%) nanoparticles recorded under various γ-irradiation doses 500 Gy, 1 kGy, 5 kGy, and 10 kGy. Each curve exhibits a single, well-defined glow peak in the 180–230 °C range, characteristic of medium-depth traps with good thermal stability and dosimetric reliability. The main glow peak positions were observed at 200 °C (500 Gy), 198 °C (1 kGy), 202 °C (5 kGy), and 221 °C (10 kGy). The minor peak shift

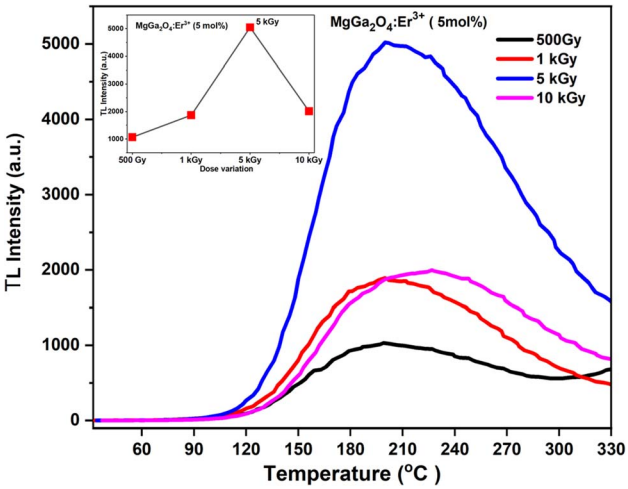

Fig. 9 Thermoluminescence (TL) glow curves of the optimal composition (5 mol% Er^{3+}) under different gamma irradiation doses (500 Gy, 1 kGy, 5 kGy and 10 kGy).

toward higher temperatures at 10 kGy indicates the creation of slightly deeper traps or trap stabilization at higher radiation doses due to increased lattice distortion and defect accumulation. The TL intensity increases proportionally with the γ-dose up to 5 kGy, where the sample exhibits the maximum luminescence output, followed by a decrease at 10 kGy. This nonlinear dose response, illustrated in the inset, reflects a typical behavior of dosimetric phosphors where trap filling efficiency and recombination probability saturate beyond an optimum dose. The initial enhancement in TL intensity with dose is attributed to the increased number of charge carriers and activation of defect-related traps such as Er^{3+}–V_0 and Er^{3+}–Ga^+ complexes. These defect centers efficiently capture electrons and holes generated during irradiation and release them upon heating, resulting in photon emission.

At low doses (500 Gy–1 kGy), only a fraction of available traps are filled, leading to relatively weak TL output. With increasing dose (up to 5 kGy), more traps are populated, improving recombination efficiency and yielding higher TL intensity. Beyond 5 kGy, the TL signal decreases, primarily due to trap saturation and recombination center depletion. At high radiation doses, excessive defect generation can lead to the formation of non-radiative centers or charge compensation effects, reducing the probability of radiative recombination. Additionally, strong ionization at higher doses can cause the merging or annihilation of existing traps, resulting in diminished TL intensity despite the increased dose. The small increase in glow peak temperature from 200 °C to 221 °C with increasing dose suggests the presence of trap redistribution where deeper traps dominate at higher irradiation levels. This indicates that prolonged exposure promotes the stabilization of Er^{3+}-associated oxygen vacancy complexes with greater trap depth (~1.1 eV), consistent with thermally stable TL behavior. The consistent, symmetric glow curve shape across all doses implies that the same type of trap center is responsible for luminescence, and only the population density changes with dose.

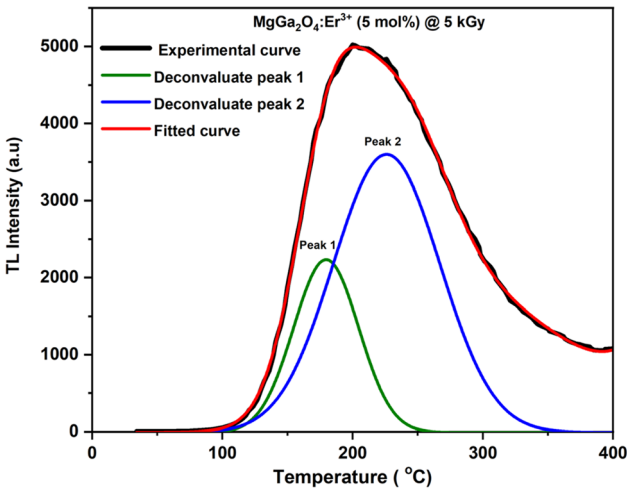

Fig. 10 Fitted thermoluminescence (TL) glow curve of $MgGa_2O_4:Er^{3+}$ (5 mol%) nanoparticles irradiated at 5 kGy, showing deconvolution into two distinct peaks.

To gain detailed insight into the nature and distribution of trapping centers in the $MgGa_2O_4:Er^{3+}$ (5 mol%) phosphor, the TL glow curve corresponding to 5 kGy γ-irradiation was deconvoluted using a general-order kinetic model, as shown in Fig. 10. The experimental glow curve (black line) was accurately resolved into two distinct overlapping peaks Peak 1 (green curve) and Peak 2 (blue curve) with an excellent fit (red curve), confirming the presence of multiple discrete trapping levels contributing to the overall TL emission behavior. The deconvoluted peaks were located at approximately 188 °C (Peak 1) and 242 °C (Peak 2), corresponding to traps of varying thermal stability. Peak 1, centered near 188 °C, represents a shallow trap with low activation energy, most likely associated with isolated oxygen vacancies (V_O), surface defects, or simple Er^{3+} substitutional sites in the spinel matrix. These shallow traps are easily emptied upon mild heating, resulting in early release of trapped charge carriers during thermal stimulation.

Peak 2, positioned around 242 °C, corresponds to a deeper, thermally stable trap and exhibits the highest intensity among the two, indicating that it is the dominant recombination center in the $MgGa_2O_4:Er^{3+}$ lattice. This peak is attributed to complex defect clusters such as Er^{3+}–V_O or Er^{3+}–Ga^{+} antisite complexes, which form stable charge-trapping sites due to local lattice distortion and charge imbalance introduced by Er^{3+} substitution. These traps possess sufficient depth to ensure prolonged charge retention and stable luminescence upon heating, making them ideal for thermoluminescent dosimetry (TLD) applications. To further understand the trap kinetics, the TL glow peaks were analyzed using the peak shape method proposed by Chen.[81] The kinetic parameters, glow peak temperature (T_m), activation energy (E), order of kinetics (b), symmetry factor (μ_g), and frequency factor (s) were determined using characteristic temperatures extracted from the TL glow curves,[82] specifically the temperatures corresponding to the half-maximum intensity on both the ascending (T_1) and descending (T_2) sides of the peak. The symmetry factor

$$\mu_g = \frac{(T_2 - T_m)}{(T_2 - T_1)} \tag{4}$$

provides information about the order of kinetics values near 0.53 indicate second-order kinetics, and intermediate values are considered general-order kinetics. The activation energy (trap depth) was calculated using the following relation from Chen's method.[83]

$$E = \frac{C_\tau (kT_m^{\,2})}{\beta} \tag{5}$$

where C_τ is a constant based on μ_g, the order of kinetics, T_m is the peak temperature in Kelvin, β is the linear heating rate (2 °C s^{-1}), and k is Boltzmann's constant (8.617×10^{-5} eV K^{-1}).[84] The frequency factor S, which describes the probability per unit time of a trapped carrier escaping, was derived from:

$$S = \frac{\beta E}{kT_m^{\,2}} \exp\left(\frac{E}{kT_m}\right) \tag{6}$$

The computed kinetic parameters for the deconvoluted peaks are presented in Table 4. The results confirm that Peak 1 corresponds to a shallow trap with relatively low activation energy (~0.83 eV), while Peak 2 is a deeper, more thermally stable trap (~0.96 eV) showing near second-order kinetics. The general-order behavior ($\mu_g \approx 0.48$–0.54) indicates a mixed trapping–detrapping process governed by multiple defect interactions within the spinel matrix. The dominance of Peak 2 suggests that the luminescent output of $MgGa_2O_4:Er^{3+}$ (5 mol%) arises primarily from deep Er^{3+}-associated traps, which release electrons upon heating and recombine radiatively through Er^{3+} 4f transitions. This process is consistent with the persistent luminescence characteristics and excellent thermal stability observed in Er^{3+}-doped spinel oxides.

The coexistence of both shallow and deep traps ensures a wide dynamic TL response range and enhances dosimetric reliability by enabling charge retention over extended periods. Hence, the kinetic analysis confirms that the dominant peak at

Table 4 TL kinetic parameters of deconvoluted peaks of $MgGa_2O_4:Er^{3+}$ (5 mol%) @ 5 kGy

Peak	T_m (°C)	Order (b)	μ_g	Activation energy (E, eV)	Frequency factor (s, s^{-1})	Remarks
1	188	1.3	0.48	0.83	1.2×10^7	Shallow trap – surface/oxygen vacancy-related
2	242	1.9	0.52	0.96	5.7×10^9	Deep, stable trap – Er^{3+}–V_O/Er^{3+}–Ga^{+} complex

242 °C, with a high activation energy and second-order kinetics, is responsible for the strong and thermally stable TL emission observed in $MgGa_2O_4$:Er^{3+} (5 mol%). These characteristics make this phosphor composition an excellent candidate for medium-dose γ-ray dosimetry and persistent luminescent applications requiring high trap stability and reproducible TL response.[85]

4 Conclusion

Er^{3+} doped $MgGa_2O_4$ nanoparticles were successfully synthesized and comprehensively characterized to elucidate their luminescent and thermoluminescent behavior. The structural analysis confirmed the retention of the cubic spinel phase upon Er^{3+} substitution, with improved crystallinity and uniform nanoscale morphology. The optical studies revealed tunable band gap and efficient visible and NIR emissions, with optimal performance observed at 3 mol% Er^{3+}, demonstrating enhanced photoluminescence lifetime and quantum yield. CIE and CCT analysis verified chromatic stability with emission located in the green–yellow region, making the material suitable for solid-state lighting. The TL response, dominated by a single glow peak near 200 °C, exhibited maximum sensitivity at 5 mol% Er^{3+} and 5 kGy dose, corresponding to medium-depth trap levels associated with Er^{3+}-induced defect complexes. TL deconvolution identified two distinct trapping centers shallow surface traps and deep intrinsic Er^{3+}–V_0/Ga^+ clusters providing stable charge storage and efficient recombination. Overall, the combination of strong photoluminescence, high color purity, and excellent thermoluminescent performance positions $MgGa_2O_4$:Er^{3+} nanoparticles as a multifunctional material for white light-emitting diodes (WLEDs) and gamma-ray dosimetry. The study establishes an important correlation between structural defects, optical transitions, and trap dynamics in Er^{3+}-doped spinel systems, offering a platform for advanced optoelectronic and radiation-sensing applications.

Author contributions

Jyothi T P: writing – original draft, conceptualization and study design, synthesis and experimental methodology, analysis and interpretation, visualization and figure preparation Kartik Gopal: writing – review & editing, synthesis and experimental methodology, data curation, analysis and interpretation. Sunitha D V: writing – review & editing, data curation, validation, supervision, formal analysis, conceptualization. Lavanya D R: formal analysis, methodology. A. P. Gnana Prakash: methodology.

Conflicts of interest

There are no conflicts to declare.

Data availability

All data generated and analyzed during this study are included in research article in the form of plots/Graphs and tables. No additional raw data are available.

Acknowledgements

The authors Kartik Gopal and Sunitha D V acknowledge REVA University for providing Seed money for the research. The authors also thank CeNSE IISc Bangalore for providing characterization facilities through INUP program. The author DVS thank VGST (ECRA/GRD No.1177/2022-23/698) for providing funding to carry out the research work.

References

1 S. P. Dhale and N. S. Ugemuge, Metal oxide-based luminescent technologies: past and future, *Luminescent Metal Oxides*, CRC Press, Boca Raton (FL), 2023, pp. 1–23.
2 K. T. Selvi and S. Sagadevan, Recent developments in optoelectronic and photonic applications of metal oxides, in *Metal Oxides for Optoelectronics and Optics-Based Medical Applications*, 2022, pp. 33–57, DOI: 10.1016/B978-0-323-85824-3.00013-0.
3 M. Shahida, S. Sagadevan, W. Ahmed, Y. Zhan, P. Opaprakasit, Metal oxides for optoelectronic and photonic applications: a general introduction, in *Metal Oxides for Optoelectronics and Optics-Based Medical Applications*, 2022, vol. 3, p. 31, DOI: 10.1016/B978-0-323-85824-3.00006-3.
4 S. Parola, B. Julián-López, L. D. Carlos and C. Sanchez, Optical properties of hybrid organic–inorganic materials and their applications, *Adv. Funct. Mater.*, 2016, **26**(36), 6506–6544.
5 A. A. Sharma, P. P. Pradhan, K. D. Prasad, M. Rakshita, R. Pembarthi and D. Haranath, Multimodal luminescence and energy transfer mechanism in narrowband UVB emitting phosphor system towards futuristic phototherapeutic devices, *Mater. Adv.*, 2025, **6**, 8400–8413, DOI: 10.1039/D5MA00810G.
6 B. Zheng, J. Fan, B. Chen, X. Qin, J. Wang and F. Wang, Rare-earth doping in nanostructured inorganic materials, *Chem. Rev.*, 2022, **122**(6), 5519–5603, DOI: 10.1021/acs.chemrev.1c00644.
7 F. Saraci, V. Quezada-Novoa, P. R. Donnarumma and A. J. Howarth, Rare-earth metal–organic frameworks: from structure to applications, *Chem. Soc. Rev.*, 2020, **49**(22), 7949–7977, DOI: 10.1039/D0CS00292E.
8 P. Su, F. Song, J. Cao, C. H. Yan and Y. Tang, Rare earth complex-based functional materials: from molecular design and performance regulation to unique applications, *Acc. Chem. Res.*, 2025, **58**(2), 218–230, DOI: 10.1021/acs.accounts.4c00649.
9 Y. Xiao, A. Feng, J. Chen, Q. Cao, L. Mi and Y. Yu, $MgGa_2O_4$-based thermal control coating: an ultra-low solar absorption coating with high irradiation stability, *Ceram. Int.*, 2024, **50**(18), 33480–33487, DOI: 10.1016/j.ceramint.2024.06.163.
10 M. A. Hamid, B. Samuels, S. Karmakar, M. A. Halim, I. H. Emu and P. K. Sarkar, Epitaxial growth and characterization of magnesium gallate ($MgGa_2O_4$) thin films by pulsed laser deposition, *J. Alloys Compd.*, 2024, **972**, 172807, DOI: 10.1016/j.jallcom.2023.172807.

11 A. Luchechko and O. Kravets, Synthesis and luminescent properties of magnesium gallate spinel doped with Mn^{2+} and Eu^{3+} ions, *Phys. Status Solidi C*, 2017, **14**(1–2), 1600146, DOI: 10.1002/pssc.201600146.

12 X. Yang, R. Zhou, H. Shi, Y. Duan and M. H. Du, Theoretical investigations of the origin of persistent luminescence in spinel oxides $MgGa_2O_4$ and $MgAl_2O_4$, *Condens. Matter.mtrl-sci.*, 2025, DOI: 10.48550/arXiv.2507.21599.

13 K. Reshu, J. Rinki, K. Pawan, S. Devender and K. Ramesh, Structural, morphological and optical characteristics of Er^{3+}doped Gd_3GaO_6 phosphor for efficient green emission in solid state lighting, *J. Mol. Struct.*, 2026, **1359**, 145495, DOI: 10.1016/j.molstruc.2026.145495.

14 Z. Ullah and R. Khan, High-temperature thermoelectric performance of spinel $MgGa_2O_4$ through a first-principles and Boltzmann transport study, *Comput. Mater. Sci.*, 2025, **259**, 114163, DOI: 10.1016/j.commatsci.2025.114163.

15 J. Tang and C. K. Duan, First-principles study on defect levels of transition metal ions in near-inverse $MgGa_2O_4$, *Opt. Mater.*, 2025, **159**, 116560, DOI: 10.1016/j.optmat.2024.116560.

16 A. Tyagi, S. Nigam, V. Sudarsan, C. Majumder, R. K. Vatsa and A. K. Tyagi, Why do relative intensities of charge transfer and intra-4f transitions of Eu^{3+} ion invert in yttrium germanate hosts? Unravelling the Underlying Intricacies from Experimental and Theoretical Investigations, *Inorg. Chem.*, 2020, **59**(17), 12659–12671, DOI: 10.1021/acs.inorgchem.0c01757.

17 M. M. M. AlmotariFabrication and characterisation of zinc oxide thin films singly doped with trace amounts of rare earth materials, PhD thesis, University of Canterbury, Christchurch, New Zealand, 2013.

18 M. K. MahataH. C. HofsässU. VetterPhoton-upconverting materials: advances and prospects for various emerging applications, in *Luminescence—An Outlook on the Phenomena and Their Applications*, 2016, pp. 109–131, DOI: 10.5772/65118.

19 L. M. Marcondes, C. R. da Cunha, B. P. de Sousa, S. Maestri, R. R. Goncalves, F. C. Cassanjes and G. Y. Poirier, Thermal and spectroscopic properties of Er^{3+}-doped and Er^{3+}/Yb^{3+} codoped niobium germanate glasses for optical applications, *J. Lumin.*, 2019, **205**, 487–494, DOI: 10.1016/j.jlumin.2018.09.046.

20 V. Hegde, K. R. Vighnesh, S. D. Kamath, C. D. Viswanath, A. H. Almuqrin and M. I. Sayyed, Near-infrared and green light emission spectroscopic characteristics of Er^{3+}-doped alumina–phosphate glasses, *Appl. Phys. A*, 2024, **130**(6), 411, DOI: 10.1007/s00339-024-07531-6.

21 T. Zhezhera, P. Gluchowski, M. Nowicki, M. Chrunik, A. Majchrowski and D. Kasprowicz, Enhanced near-infrared emission of Er^{3+} as a synergistic effect of energy transfers in Bi_3TeBO_9:Yb^{3+},Er^{3+} phosphors, *J. Lumin.*, 2023, **258**, 119774, DOI: 10.1016/j.jlumin.2023.119774.

22 S. Shen and A. Jha, Influence of F^--ion doping on fluorescence ($^4I_{13/2} \rightarrow {}^4I_{15/2}$) line-shape broadening in Er^{3+}-doped oxyfluoride silicate glasses, *Opt. Mater.*, 2004, **25**(3), 321–333, DOI: 10.1016/j.optmat.2003.08.006.

23 A. Herrmann and D. Ehrt, Green and red Er^{3+} photoluminescence behavior in various fluoride glasses, *Int. J. Appl. Glass Sci.*, 2010, **1**(4), 341–349, DOI: 10.1111/j.2041-1294.2010.00031.x.

24 A. A. Kaminskii, A. G. Petrosyan, G. A. Denisenko, T. I. Butaeva, V. A. Fedorov and S. E. Sarkisov, Spectroscopic properties and 3 μm stimulated emission of Er^{3+} ions in $(Y_1-xEr_x)_3Al_5O_{12}$ and $(Lu_1-xEr_x)_3Al_5O_{12}$ garnet crystals, *Phys. Status Solidi A*, 1982, **71**(2), 291–312, DOI: 10.1002/pssa.2210710202.

25 E. Y. Rostokina, A. D. Plekhovich, A. M. Kutin, I. F. Georgiu, S. S. Balabanov and M. E. Komshina, Kinetic effects of Er^{3+} substitution for Y^{3+} in $(Y_1-xEr_x)_3Al_5O_{12}$ garnet, *J. Eur. Ceram. Soc.*, 2021, **41**(10), 5324–5330, DOI: 10.1016/j.jeurceramsoc.2021.03.065.

26 R. Kiran, N. Kamath, M. I. Sayyed, A. H. Almuqrin and S. D. Kamath, Recent developments in rare-earth-doped nanophosphors for emerging technological applications, *RSC Adv.*, 2025, **15**(25), 20040–20060, DOI: 10.1039/D5RA03126E.

27 X. Zhao, S. He and M. C. Tan, Design of infrared-emitting rare-earth-doped nanoparticles and nanostructured composites, *J. Mater. Chem. C*, 2016, **4**(36), 8349–8372, DOI: 10.1039/C6TC02373H.

28 G. Pu, J. Song, Z. Cheng, Y. Tang, C. Kang and J. Wang, Interfacial Molecular Engineering of Rare Earth-Doped Nanocrystals: Basic Principles, Construction Strategies, and Advanced Applications, *Laser Photonics Rev.*, 2025, 2500156, DOI: 10.1002/lpor.202500156.

29 N. O. Etafo, Advancements of lanthanide-doped phosphors in solid-state lighting applications, *Curr. Phys.*, 2024, **1**(1), E220124225904, DOI: 10.2174/0127723348280880240115054806.

30 R. Sun, D. Zhou and H. Song, Rare-earth doping in perovskite luminescent nanocrystals and photoelectric devices, *Nano Select*, 2022, **3**(3), 531–554, DOI: 10.1002/nano.202100187.

31 A. Lakshmanan, Role of sintering in the synthesis of luminescence phosphors, *Sintering of Ceramics—New Emerging Techniques*, 2012, pp. 323–356.

32 S. Singh, D. Singh, P. Siwach, I. Gupta and P. Kumar, Synthesis strategies for rare-earth-activated inorganic phosphors: a mini-review, *Appl. Res.*, 2025, **4**(1), e202400190, DOI: 10.1002/appl.202400190.

33 K. Gopal, D. V. Sunitha and M. Ranot, Surface-engineered Dy_2O_3 nanoparticles: A comparative study of pure and PVP-coated Dy_2O_3 nanoparticles variants for high-fidelity photoluminescence, latent fingerprinting, anti-counterfeiting and solid-state lighting applications, *Surf. Interfaces*, 2025, 106741, DOI: 10.1016/j.surfin.2025.106741.

34 K. Gopal and D. V. Sunitha, PVP-functionalized Dy_2O_3/Pr_2O_3 nanocomposites for photoluminescence, WLEDs, latent fingerprinting, and anti-counterfeiting, *RSC Adv.*, 2025, **15**(42), 35553–35565, DOI: 10.1039/D5RA06661A.

35 T. P. Jyothi, K. Gopal, D. V. Sunitha and R. Venkatesh, Gd_2O_3Nanoarchitectures: Orchestrating radiant tales with Dy^{3+}, Eu^{3+}, Pr^{3+}, and Sm^{3+} for cutting-edge

photoluminescence and forensic applications, *Ceram. Int.*, 2025, **51**(6), 7946–7963, DOI: 10.1016/j.ceramint.2024.12.232.

36 L. Ren, D. Wang, D. Yang, G. Sun, H. Xu and J. Xuan, Tunable Cr^{3+}–Cr^{3+} ion-pair luminescence in $MgGa_2O_4$:Cr^{3+} NIR phosphors via alkaline-earth co-doping, *J. Photochem. Photobiol., A*, 2025, 116612, DOI: 10.1016/j.jphotochem.2025.116612.

37 H. Xiang, R. Wang, J. Chen, F. Li and H. Zeng, Research progress of full electroluminescent white light-emitting diodes based on a single emissive laye, *Light Sci. Appl.*, 2021, **10**(1), 206, DOI: 10.1038/s41377-021-00640-4.

38 R. Priya, S. Angaria, S. Singh, R. Gopal, V. Dubey and M. B. Latif, in *Introduction to Luminescence and Luminescent Materials, Luminescence Spectroscopy and Microscopy*, Springer, Cham, 2026, 08745-4_1, DOI: 10.1007/978-3-032-08745-4_1.

39 Z. Shi, S. Li, Z. Zheng, X. Feng, Z. Fang, J. Yang and B. Tang, Crystal structure, microstructure, and microwave dielectric properties of $MgGa_2O_4$ and $ZnGa_2O_4$ ceramics prepared by reaction sintering, *J. Electron. Mater.*, 2024, **53**(5), 2240–2249, DOI: 10.1007/s11664-024-10928-x.

40 D. V. Mlotswa, L. L. Noto, S. J. Mofokeng, K. O. Obodo, V. R. Orante-Barrón and B. M. Mothudi, Luminescence dynamics of $MgGa_2O_4$ prepared by solution combustion synthesis, *Opt. Mater.*, 2020, **109**, 110134, DOI: 10.1016/j.optmat.2020.110134.

41 A. Babu and N. M. Rao, Effect of copper substitution on structural, optical, and magnetic properties of β-Ga_2O_3 powders, *Appl. Phys. A*, 2025, **131**(3), 172, DOI: 10.1007/s00339-025-08293-5.

42 Z. Fatima, R. Y. Khosa, I. Safra, T. R. Aldhafeeri, S. K. Ali, A. Kumar and M. R. Karim, Enhancing electrochemical efficiency of rGO-supported Er_2O_3 electrocatalyst for water splitting, *Eur. Phys. J.*, 2025, **140**(6), 596, DOI: 10.1140/epjp/s13360-025-06507-6.

43 U. Holzwarth and N. Gibson, The Scherrer equation versus the Debye–Scherrer equation, *Nat. Nanotechnol.*, 2011, **6**(9), 534, DOI: 10.1038/nnano.2011.145.

44 S. Mustapha, M. M. Ndamitso, A. S. Abdulkareem, J. O. Tijani, D. T. Shuaib, A. K. Mohammed and A. Sumaila, Comparative study of crystallite size using Williamson–Hall and Debye–Scherrer plots for ZnO nanoparticles, *Adv. Nat. Sci. Nanosci. Nanotechnol.*, 2019, **10**(4), 045013, DOI: 10.1088/2043-6254/ab52f7.

45 A. O. Bokuniaeva and A. S. Vorokh, Estimation of particle size using the Debye equation and the Scherrer formula for polyphasic TiO_2 powder, *J. Phys., Conf. Ser.*, 2019, **1410**(1), 012057, DOI: 10.1088/1742-6596/1410/1/012057.

46 A. R. Bushroa, R. G. Rahbari, H. H. Masjuki and M. R. Muhamad, Approximation of crystallite size and microstrain via XRD line-broadening analysis in TiSiN thin films, *Vacuum*, 2012, **86**(8), 1107–1112, DOI: 10.1016/j.vacuum.2011.10.011.

47 D. J. Robbins and P. J. Dean, The Effects of core structure on radiative and non-radiative recombinations at metal ion substituents in semiconductors and phosphors, *Adv. Phys.*, 1978, **27**(4), 499–532, DOI: 10.1080/00018737800101434.

48 R. V. Rossel, R. N. McGlynn and A. B. McBratney, Determining the composition of mineral–organic mixes using UV–vis–NIR diffuse reflectance spectroscopy, *Geoderma*, 2006, **137**(1–2), 70–82, DOI: 10.1016/j.geoderma.2006.07.004.

49 P. R. Jubu, O. S. Obaseki, D. I. Ajayi, E. Danladi, K. M. Chahrour and A. Muhammad, Considerations about the determination of optical bandgap from diffuse reflectance spectroscopy using the tauc plot, *J. Opt.*, 2024, **53**(5), 5054–5064, DOI: 10.1007/s12596-024-01741-0.

50 L. S. Amrut and P. Shinde, A Review of Novel Phosphor Solutions and Their Applications in White LED Technology, *Int. J. Technol. Res.*, 2024, **12**(4), 107–114.

51 J. U. Rahman, S. Khan, V. Jain, A. Rajiv, S. Dasi and K. F. Fawy, Exploring inorganic phosphors: basics, types, fabrication and luminescence properties for LED/WLED/displays, *Rev. Inorg. Chem.*, 2025, **45**(1), 55–76, DOI: 10.1515/revic-2024-0044.

52 S. Wu, J. Xue, R. Wang and J. Li, Synthesis, Characterization and Microwave Dielectric Properties of Spinel MgGa2O4 Ceramic Materials, *J. Alloys Compd.*, 2014, **585**, 542–548, DOI: 10.1016/j.jallcom.2013.09.176.

53 S. M. Ngaram, S. Hashim, M. S. M. Sanusi, A. Ibrahim and M. I. Sayyed, Structural and optical characteristics of B_2O_3–TeO_2–Bi_2O_3–$SrCO_3$–K_2CO_3–Er_2O_3 glass systems: role of Er^{3+} doping, *Ceram. Int.*, 2025, **51**(5), 5882–5889, DOI: 10.1016/j.ceramint.2024.12.033.

54 T. P. Jyothi, K. Gopal, D. V. Sunitha, D. Kavyashree and A. P. G. Prakash, Optical tuning and dual luminescence behavior of $MgGa_2O_4$:Dy^{3+} for optoelectronic and dosimetric applications, *Ceram. Int.*, 2025, **51**(26 Pt C), 50644–50657, DOI: 10.1016/j.ceramint.2025.08.293.

55 Y. Kong, H. Chen and L. Zuo, Understanding the Nonradiative Charge Recombination in Organic Photovoltaics: From Molecule to Device, *Adv. Funct. Mater.*, 2025, **35**(3), 2413864, DOI: 10.1002/adfm.202413864.

56 P. Meejitpaisan, R. Doddoji, S. Kothan, H. J. Kim and J. Kaewkhao, Near-UV-excited photoluminescence of Dy^{3+}-doped oxyfluoride–phosphosilicate glasses for natural white light generation, *Chem. Phys.*, 2025, 112860, DOI: 10.1016/j.chemphys.2025.112860.

57 J. Li, B. Wei, Y. Chen, M. Zhang, P. Ren and M. Wang, Er^{3+}:$Cs_2AgInCl_6$ double perovskites with strain-engineered broadband emission for flexible night-vision films, *J. Alloys Compd.*, 2025, 184371, DOI: 10.1016/j.jallcom.2025.184371.

58 N. Y. Elsheikh, M. S. Shams, A. A. Arais and I. K. Battisha, Tailored photonic properties of Er/Yb/Fe/Co/Ni co-doped ZnO thin films for integrated planar waveguide applications, *Surf. Interfaces*, 2025, 107834, DOI: 10.1016/j.surfin.2025.107834.

59 S. N. Nazrin, M. S. Sutrisno, H. B. Zaman, N. Jothi, A. Assaiqeli and S. Ezzine, Enhanced photoluminescence and optical properties of erbium-doped zinc tellurite glasses for visible and near-infrared photonic applications,

J. Lumin., 2025, **281**, 121184, DOI: 10.1016/j.jlumin.2025.121184.

60 Y. Yang, C. Cen, L. Kan, Q. Zhao, Z. Huang and S. Li, Organic probes for three-photon fluorescence imaging in the NIR-II window: design, applications and perspectives, *Interdiscip. Mater.*, 2025, **4**(1), 109–137, DOI: 10.1002/idm2.12217.

61 W. Thor, J. C. G. Bünzli, K. L. Wong and P. A. Tanner, Shedding Light on Luminescence Lifetime Measurement and Associated Data Treatment, *Adv. Photonics Res.*, 2025, **6**(2), 2400081, DOI: 10.1002/adpr.202400081.

62 Y. Yuan, G. Yan, C. Dreessen and T. Kirchartz, Understanding power-law photoluminescence decays and bimolecular recombination in lead-halide perovskites, *Adv. Energy Mater.*, 2025, **15**(6), 2403279, DOI: 10.1002/aenm.202403279.

63 S. Liu, Long-lived optical coherence and spin lifetimes in Eu^{3+}:Y_2O_3 oxide ceramics for quantum memories, *Commun. Phys.*, 2025, **8**(1), 338, DOI: 10.1038/s42005-025-02259-y.

64 M. A. Behrens, A. Franzén, S. Carlert, U. Skantze, L. Lindfors and U. Olsson, On the Ostwald ripening of crystalline and amorphous nanoparticles, *Soft Matter*, 2025, **21**(12), 2349–2354, DOI: 10.1039/D4SM01544D.

65 K. Gopal, D. V. Sunitha and M. Ranot, Surface-engineered Dy_2O_3 nanoparticles: comparative study of pure and PVP-coated variants for photoluminescence, latent fingerprinting, anti-counterfeiting, and solid-state lighting, *Surf. Interfaces*, 2025, 106741, DOI: 10.1016/j.surfin.2025.106741.

66 K. Gopal and D. V. Sunitha, PVP-functionalized Dy_2O_3/Pr_2O_3 nanocomposites for photoluminescence, WLEDs, latent fingerprinting, and anti-counterfeiting, *RSC Adv.*, 2025, **15**(42), 35553–35565, DOI: 10.1039/D5RA06661A.

67 S. Wu, L. G. Teoh, K. T. Liu and Y. S. Chang, Synthesis and photoluminescence properties of $MgGa_2O_4$:Dy^{3+} phosphor under different wavelength excitation, *J. Electron. Mater.*, 2025, **54**, 4718–4725, DOI: 10.1007/s11664-025-11896-6.

68 A. Romanov, E. Haula, A. V. Kapustin, A. Kostyukov, A. Egorov, V. Kuzmin and V. Korchak, Near-IR photoluminescence from Cu^{2+} impurity in $LiAl_5O_8$ and in $MgAl_2O_4$, $ZnAl_2O_4$, $MgGa_2O_4$, $ZnGa_2O_4$ spinels, *Opt. Mater.*, 2026, **105**, 112614, DOI: 10.1016/j.optmat.2025.117808.

69 X. Z. Yang, T. Q. Zhao, R. Abdurahman, S. J. Liu, Y. X. Han and Y. Zhang, Ratiometric temperature sensing with non-thermally coupled levels from Pr–Al co-doped $MgGa_2O_4$, *J. Solid State Chem.*, 2025, **341**, 125043, DOI: 10.1016/j.jssc.2024.125043.

70 F. Zhang, J. Zhang and X. Zhang, Maximum luminance prediction for multichannel LED light sources under chromaticity constraints for tunable lighting, *Opt. Express*, 2025, **33**(17), 36343–36357, DOI: 10.1364/OE.572221.

71 B. Tasci and Y. Erol, Innovative Approach to Adjustable Color Temperature in LED Luminaires, *Firat. Univ. J. Exp. Comp. Eng.*, 2025, **4**(2), 245–261, DOI: 10.62520/fujece.1537662.

72 I. Fryc and M. Listowski, Energy efficiency versus color consistency in LED lighting, *Energies*, 2025, **18**(17), 4482, DOI: 10.3390/en18174482.

73 J. Y. Ren, S. Y. Xie, X. Y. Ma, J. Z. Xue, X. M. Li, C. L. Lu and Y. Duan, Dopant-free organic light-emitting devices with low blue hazard, low color temperature, and high color rendering index, *Opt. Express*, 2025, **33**(7), 16161–16173, DOI: 10.1364/OE.550424.

74 R. Liu, Z. Yan, T. Lu, G. Chen, J. Zheng and S. Wang, Emerging perovskite color converters for next-generation wireless communications, *Microstructures*, 2025, **5**(3), DOI: 10.20517/microstructures.2024.142.

75 C. K. Shilpa, S. V. Jasira, V. P. Veena, S. V. Sajith, A. M. Huda Thasneem and K. Greeshma, Thermally stable Sm^{3+}-doped $SrCeO_3$ single-phase white phosphor with Y^{3+} sensitization for WLEDs, *Sci. Rep.*, 2025, **15**(1), 24205, DOI: 10.1038/s41598-025-09142-4.

76 A. Marngar and V. Dubey, Thermoluminescence (TL) properties of quartz from different geological settings and their implications for geological dating and radiation dosimetry, *J. Radioanal. Nucl. Chem.*, 2025, **334**, 7599–7621, DOI: 10.1007/s10967-025-10464-w.

77 S. A. Nouh, E. E. Alghamdi, N. S. Gaballah, S. S. Eldera, F. AlSomali, K. A. Benthami and M. M. E. Barakat, Tailoring the optical and color properties of gamma-irradiated PC/CuO nanocomposite films for their application in optoelectronic devices, *Radiat. Eff. Defects Solids*, 2025, **180**(1–2), 209–226, DOI: 10.1080/10420150.2025.2475370.

78 S. Zhang, F. Zhao, S. Liu, Z. Song and Q. Liu, An Improved evaluation of trap depth from thermoluminescence, *J. Rare Earths*, 2025, **43**(2), 262–269, DOI: 10.1016/j.jre.2024.02.004.

79 S. Yeshodamma, K. Hareesh, H. Nagabhushana, J. Dwivedi, V. C. Petwal and D. V. Sunitha, Influence of electron beam irradiation on structural, thermo and photoluminescence properties of $SrTiO_3$:Sm^{3+} nanophosphor, *Optik*, 2020, **223**, 165483, DOI: 10.1016/j.ijleo.2020.165483.

80 L. V. Vikas, R. K. Tamrakar and S. Butolia, Thermoluminescence glow-curve study of UV-irradiated Mn^{4+}-doped zinc aluminate spinel nanophosphor, *J. Mater. Sci. Mater. Electron.*, 2025, **36**(2), 171, DOI: 10.1007/s10854-025-14229-9.

81 W. Zheng, J. Yu, F. Zhu, C. Wang, M. Chen and F. Luo, Luminescence and thermoluminescence of a new long-afterglow phosphor $Na_2Ca_2CeS_2Si_3O_{12}$ for AC-LED applications, *Ceram. Int.*, 2025, **51**, 63793–63801, DOI: 10.1016/j.ceramint.2025.11.008.

82 Y. D. Narad, Y. R. Parauha, N. G. Nikolay and S. J. Dhoble, Radiation-induced Y_2O_3:Eu phosphor: thermoluminescence characterization and trapping parameter investigations, *J. Mater. Sci. Mater. Electron.*, 2025, **36**(8), 470, DOI: 10.1007/s10854-025-14505-8.

83 Y. Wang, L. Wang, A. Li, N. Li, Y. Cao and X. Wang, Organic thermoluminescence driven by electron back transfer: microsecond explosive emission to persistent multi-hour afterglow, *Adv. Mater.*, 2025, e08292, DOI: 10.1002/adma.202508292.

84 P. D. Townsend, Y. Wang and S. W. S. McKeever, Thermoluminescence, a Critical Reappraisal of Successes, Uncertainties, and a Look to the Future, *Photonics*, 2025, **13**(1), 29, DOI: 10.3390/photonics13010029.

85 D. Toktamis, S. Iflazoglu, H. Toktamis, A. Yılmaz and A. N. Yazıcı, Effect of Ag Doping on Thermoluminescence Properties and Radiation Dosimetry Performance of MgB_4O, *Luminescence*, 2025, **40**(10), e70341, DOI: 10.1002/bio.70341.